Molecular Cancer

RESEARCH Open Access

YTHDF2 in peritumoral hepatocytes mediates chemotherapy-induced antitumor immune responses through CX3CL1-mediated CD8$^+$ T cell recruitment

Zhenyun Yang[1,2,3†], Xin Wang[1,2,3†], Yizhen Fu[1,2,3†], Weijie Wu[1,2,3†], Zili Hu[1,2,3], Qingyang Lin[1,2,3], Wei Peng[1,2,3], Yangxun Pan[1,2,3], Juncheng Wang[1,2,3], Jinbin Chen[1,2,3], Dandan Hu[1,2,3], Zhongguo Zhou[1,2,3], Li Xu[1,2,3], Yaojun Zhang[1,2,3], Jiajie Hou[4,5*] and Minshan Chen[1,2,3*]

Abstract

Peritumoral hepatocytes are critical components of the liver cancer microenvironment, However, the role of peritumoral hepatocytes in the local tumor immune interface and the underlying molecular mechanisms have not been elucidated. YTHDF2, an RNA N^6-methyladenosine (m^{6}A) reader, is critical for liver tumor progression. The function and regulatory roles of YTHDF2 in peritumoral hepatocytes are unknown. This study demonstrated that oxaliplatin (OXA) upregulated m^{6}A modification and YTHDF2 expression in hepatocytes. Studies using tumor-bearing liver-specific *Ythdf2* knockout mice revealed that hepatocyte YTHDF2 suppresses liver tumor growth through CD8$^+$ T cell recruitment and activation. Additionally, YTHDF2 mediated the response to immunotherapy. Mechanistically, OXA upregulated YTHDF2 expression by activating the cGAS-STING signaling pathway and consequently enhanced the therapeutic outcomes of immunotherapeutic interventions. Ythdf2 stabilized *Cx3cl1* transcripts in an m^{6}A-dependent manner, regulating the interplay between CD8$^+$ T cells and the progression of liver malignancies. Thus, this study elucidated the novel role of hepatocyte YTHDF2, which promotes therapy-induced antitumor immune responses in the liver. The findings of this study provide valuable insights into the mechanism underlying the therapeutic benefits of targeting YTHDF2.

†Zhenyun Yang, Xin Wang, Yizhen Fu and Weijie Wu contributed equally to this work.

*Correspondence:
Jiajie Hou
jiajiehou@um.edu.mo
Minshan Chen
chenmsh@sysucc.org.cn
[1]Department of Liver Surgery, Sun Yat-sen University Cancer Center, Guangzhou, Guangdong 510060, People's Republic of China
[2]Collaborative Innovation Center for Cancer Medicine, State Key Laboratory of Oncology in South China, Sun Yat-Sen University Cancer Center, Guangzhou, Guangdong 510060, People's Republic of China
[3]State Key Laboratory of Oncology in South China, Guangdong Provincial Clinical Research Center for Cancer, Collaborative Innovation Center for Cancer Medicine, Sun Yat-Sen University Cancer Center, Guangzhou 510060, Guangdong, China
[4]Cancer Centre, Faculty of Health Sciences, University of Macau, Macau, SAR, China
[5]MOE Frontier Science Centre for Precision Oncology, University of Macau, Macau, SAR, China

Introduction

Liver cancer is a prevalent malignancy worldwide and the third most common cause of cancer-related mortality [1]. Apart from hepatic primary malignancies, liver also remains persistently susceptible to colonization by metastatic lesions arising from diverse organ sites (most notably colon cancer), it's reported that half of colorectal cancer patients were accompanied with liver metastasis at first diagnose and finally died due to intra-hepatic tumor progression [2, 3]. Recent studies have suggested that hepatocytes, which are essential components of the liver tumor microenvironment (TME), are associated with liver cancer development and progression [3, 4]. However, the functional role and clinical importance of hepatocytes in liver malignancy have not been previously examined. Hepatocytes along with immunocytes form the TME. Tumorigenesis is proposed to involve the recruitment of lymphocytes. However, the interaction between hepatocytes, lymphocytes, and cancer cells is unclear. Thus, there is an urgent need to elucidate the molecular mechanism underlying liver cancer progression to develop novel therapeutic strategies.

N^6-methyladenosine (m^6A) methylation, a common epigenetic RNA modification, can regulate various molecular and cellular processes modulating the infiltration and activation of tumor-infiltrating lymphocytes (TILs) [5]. Additionally, chemotherapy agents can regulate RNA m^6A modification in tumor cells, suppressing tumor progression and immune escape through various mechanisms, including the induction of immunogenic alterations [6, 7]. Oxaliplatin (OXA)-based chemotherapy has been used as a standard therapeutic modality in the management of liver cancer and colorectal cancer (CRC) [8–10]. Several studies have indicated that OXA-based chemotherapy in combination with immunotherapy increases the survival duration of patients with advanced hepatocellular carcinoma (HCC) and CRC [11–14]. Chemotherapy elicits antitumor immune responses through the induction of immunogenic cell death and the disruption of immune evasion by tumor cells [15, 16]. The mechanisms underlying the modulation of the liver immune microenvironment and the enhanced tumor response after treatment with the combination of OXA and immunotherapy have not been elucidated.

YTHDF2, a known m^6A (N^6-methyladenosine) reader, modulates mRNA stability and is hypothesized to function as a tumor suppressor [17]. Previous studies have reported that YTHDF2 is associated with TILs in different types of cancer. In lower-grade glioma or kidney renal clear cell carcinoma, YTHDF2 expression is positively correlated with the infiltration of B cells, $CD8^+$ T cells, $CD4^+$ T cells, macrophages, neutrophils, and dendritic cells (DCs) [18, 19]. Additionally, YTHDF2 expression is positively correlated with the infiltration of $CD8^+$ T cells, $FOXP3^+$ T cells, PD-1^+ T cells, and $CD45RO^+$ immune cells in non-small-cell lung cancer [20]. Furthermore, YTHDF2 deficiency in tumor-associated macrophages (TAMs) suppressed tumor growth by reprogramming TAMs toward an antitumoral phenotype, enhancing $CD8^+$ T cell-mediated antitumor immunity [21]. Recently, we demonstrated that YTHDF2 downregulation promotes inflammation and aberrant vascular remodeling in HCC [22]. However, the function of YTHDF2 in peritumoral hepatocytes is unknown. A recent study demonstrated that alterations in normal hepatocytes modulate the progression of liver cancer [23]. The regulatory mechanisms underlying the interaction between OXA and YTHDF2 have not been elucidated.

In this study, we revealed that YTHDF2 in hepatocytes which could be up-regulated by OXA played a pivotal role in impeding the progression of liver cancer. Hepatic YTHDF2 was essential for the maintenance of antitumor response in the liver. The loss of YTHDF2 in hepatocytes decreased the stability of *CX3CL1* mRNA, impairing $CD8^+$ T cell function and promoting tumor growth in both mouse models and patients with HCC. OXA upregulated the activation of the transcription factor IRF3 in hepatocytes, which resulted in the upregulation of YTHDF2 and downstream biological processes. Finally, this study demonstrated that the YTHDF2-CX3CL1 axis in hepatocytes enhances the antitumor efficacy of immunotherapy.

Results

OXA upregulates YTHDF2 in peritumoral hepatocytes and YTHDF2 upregulation is associated with improved survival outcomes

This study examined the effects of chemotherapy on the RNA m^6A levels in hepatocytes. The RNA m^6A levels in the peritumoral tissues were compared between patients with HCC who received OXA-based hepatic arterial infusion chemotherapy (HAIC) and treatment-naïve patients using the dot blot assay. HAIC was administered as described previously [24, 25]. The hepatocyte RNA m^6A levels in patients treated with OXA were markedly upregulated when compared with those in treatment-naïve patients (Fig. 1a). Analysis of the hepatic RNA m^6A levels in C57BL/6 mice treated with or without OXA revealed similar findings (Supplementary Fig. 1a). Thus, OXA-based chemotherapy upregulates the RNA m^6A level in hepatocytes.

Quantitative real-time polymerase chain reaction (qRT-PCR) analysis revealed that OXA modulated the hepatic expression levels of m^6A-associated genes in patients with HCC and the mouse model. In particular, YTHDF2 was the most significantly upregulated gene (Fig. 1b and Supplementary Fig. 1b). Immunoblotting (Fig. 1c and Supplementary Fig. 1c) and immunohistochemical

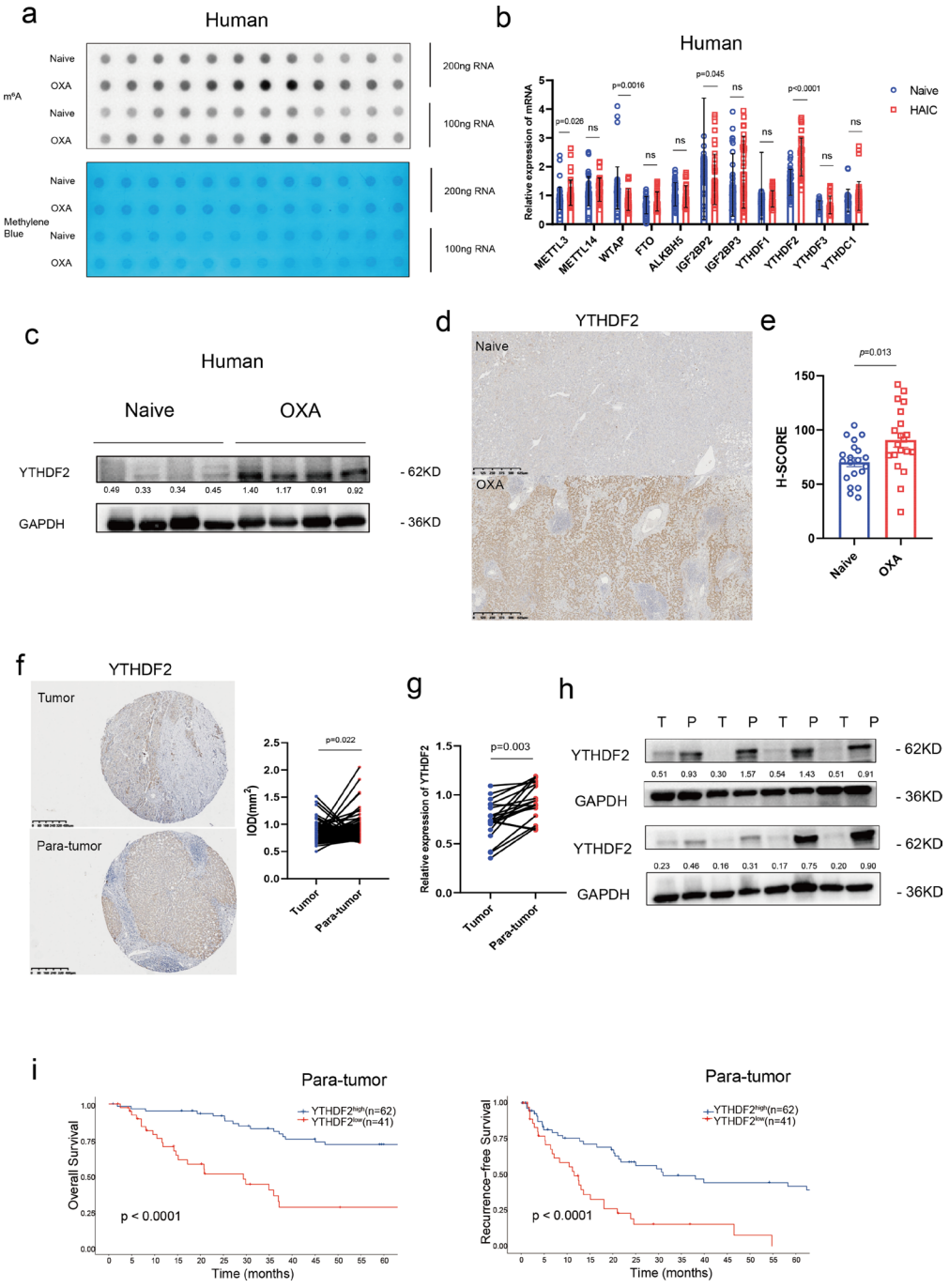

Fig. 1 OXA upregulates YTHDF2 in peritumoral hepatocytes and YTHDF2 upregulation is associated with improved survival outcomes. **a**, The m^{6}A level of peritumoral tissues from treatment naive HCC patients and HCC patients treated with hepatic arterial infusion chemotherapy (HAIC) with oxaliplatin (OXA) was indicated by m^{6}A dot blot. Corresponding RNAs were loaded equally by a 2-fold serial dilution with 200 ng and 100 ng. Methylene blue staining served as a loading control ($n=6$). **b**, Relative mRNA levels of genes associated with m^{6}A in treatment naive HCC patients and HCC patients treated with OXA, as assessed by RT-qPCR ($n=16$, performed in triplicate). **c**, Immunoblot of YTHDF2 in peritumoral tissues from treatment naive HCC patients and HCC patients treated with HAIC ($n=4$). **d**, Immunohistological staining of YTHDF2 in peritumoral tissues from treatment naive HCC patients and HCC patients treated with HAIC. **e**, Histochemistry score (H-SCORE) value of YTHDF2 in peritumoral tissues from treatment naive HCC patients and HCC patients treated with HAIC ($n=20$). **f**, Immunohistological staining of YTHDF2 in human HCC tissue microarrays, and IOD value of YTHDF2 in paired tumor and peritumoral tissues of treatment-naïve patients ($n=103$).**g**, RT-qPCR of YTHDF2 in paired tumor (T) and peritumoral (P) tissues of treatment-naïve patients ($n=20$) **h**, Immunoblot of YTHDF2 in paired tumor (T) and peritumoral (P) tissues ($n=8$). **i**, Kaplan-Meier analyses of the correlation between YTHDF2 expression level in pare-tumor tissues and overall survival (left) or recurrence-free survival (right) in treatment-naive HCC patients ($n=103$ in total). Error bars indicate means ± SD. P-values were determined by an unpaired two-tailed t-test (**b**, **e**). P-values were determined by a paired two-tailed t-test (**g**). P-values were calculated using the log-rank test (**i**). Data in a-h are representative of at least two independent experiments. ns, not significant

(Fig. 1d-e) analyses revealed that OXA upregulated the protein level of YTHDF2 in the liver tissues of both patients with HCC and mice. These results suggest that OXA promotes the transcription of *Ythdf2*.

The mRNA and protein levels of YTHDF2 in tumor tissues were lower than those in peritumoral tissues in treatment-naïve patients (Fig. 1f–h). Therefore, this study examined the correlation between hepatocyte YTHDF2 expression and the survival of patients with HCC. As shown in Fig. 1i and Supplementary Table 1, YTHDF2 upregulation was significantly correlated with increased overall and recurrence-free survival in a cohort of 103 patients with HCC (recruited from 2008 to 2014). Moreover, in patients receive OXA treatment, the expression of YTHDF2 in tumor tissues were lower than those in peritumoral tissues (Supplementary Fig. 1d). YTHDF2 upregulation was significantly correlated with good prognosis in patients with HCC received OXA treatment (Supplementary Fig. 1e). These results suggest that OXA upregulated YTHDF2 expression in hepatocytes and that YTHDF2 upregulation is associated with improved survival.

OXA activates *Ythdf2* transcription in hepatocytes through cGAS-STING signaling

We have demonstrated that OXA could enhance the transcription of *Ythdf2* in mouse and human liver tissues. Similarly, we observed that expression of YTHDF2 was also increased in AML12 cells (the mouse hepatocyte cell line) treated with OXA (Fig. 2a and Supplementary

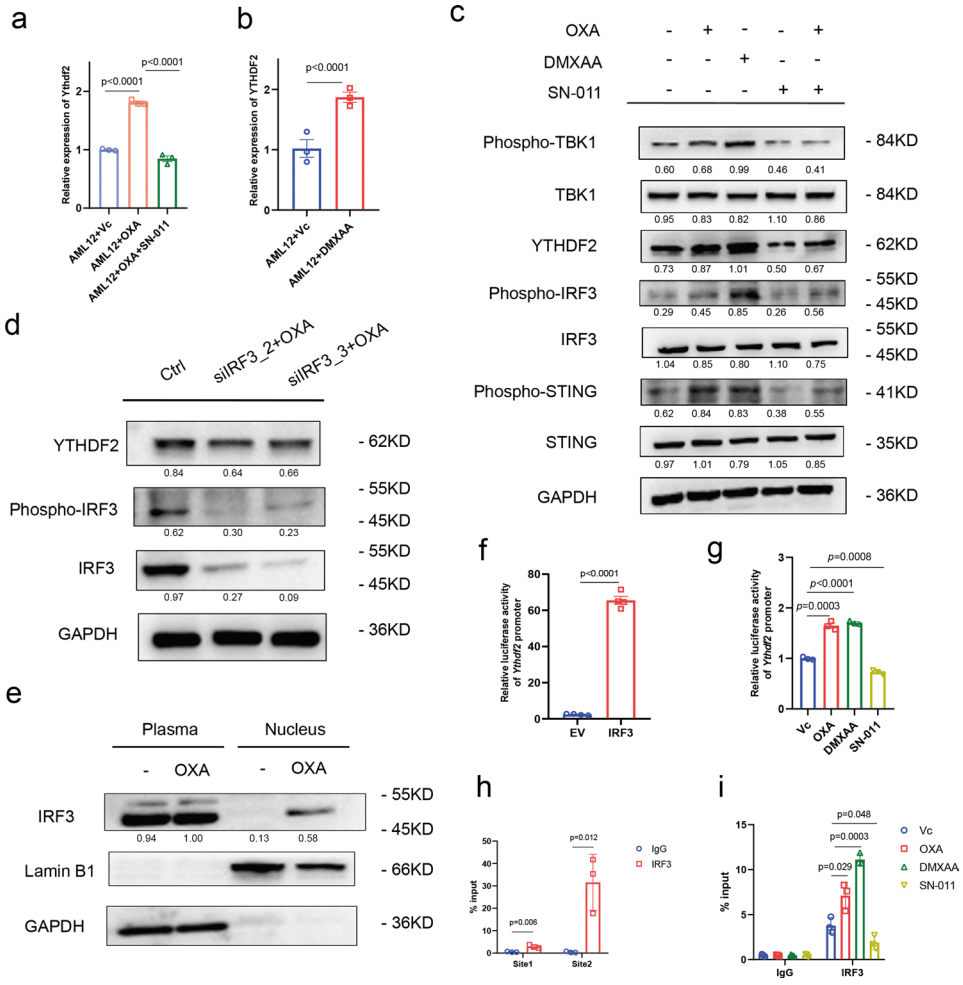

Fig. 2 OXA activates *Ythdf2* transcription in hepatocytes through cGAS-STING signaling. **a**, **b**,**c**, qRT-PCR (**a**, **b**) and immunoblotting (c) showing the expression of YTHDF2 in AML12 cells treated with vehicle, OXA, SN-011 (cGAS-STING inhibitor) and DMXAA (cGAS-STING agonist) ($n=3$). **d**, immunoblotting showing the expression of YTHDF2 in AML12-siCtrl, AML12-siIRF3_2 and AML12-siIRF3_3 cells treated with OXA. **e**, immunoblotting showing expression of IRF3 in plasma and nucleus of AML12 treated with OXA. **f**, Relative luciferase activity of constructs containing *Ythdf2* promoter in AML12 cells transfected with IRF3 expressing plasmid or empty vector ($n=4$). **g**, Relative luciferase activity of constructs containing *Ythdf2* promoter in AML12 cells treated with vehicle, OXA, SN-011 and DMXAA ($n=3$). **h**, ChIP-qPCR showing the binding of IRF3 to the *Ythdf2* promoter in AML12-oeIRF3 cells ($n=3$). **i**, ChIP-qPCR showing the enrichment of the *Ythdf2* promoter in AML12 cells treated with vehicle, OXA, SN-011 and DMXAA ($n=3$). Error bars indicate means ± SD. P-values were determined by an unpaired two-tailed t-test (**a**, **b**,**f**-**i**). Data in **a**-**i** are representative of at least two independent experiments

Fig. 2a). In contrast, fluorouracil, another chemotherapeutic agent used in HAIC, did not affect the expression of YTHDF2 in vitro (Supplementary Fig. 2b–c) and in vivo (Supplementary Fig. 2d). Next, the mechanism of OXA-induced YTHDF2 upregulation in hepatocytes was examined. Previous studies have indicated that OXA activates the cGAS-STING signaling in different cell types [26, 27]. However, the mechanism of OXA in the liver is unknown. OXA and DMXAA (cGAS-STING agonist) upregulated cGAS-STING pathway activation and YTHDF2 expression, whereas SN-011 (cGAS-STING inhibitor) mitigated the OXA-induced and DMXAA-induced upregulation of cGAS-STING pathway activation and YTHDF2 expression (Fig. 2a–c). To determine the upstream transcription factor of YTHDF2, the putative transcription factors were examined in ChIPBase and the Animal Transcription Factor Database. IRF3, a critical transcription factor in the cGAS-STING signaling pathway, could potentially bind to YTHDF2 and directly regulate YTHDF2 expression. Then we conducted the *Irf3* knockdown AML12 cells (Supplementary Fig. 2e–f) and observed that OXA did not upregulate YTHDF2 expression in *Irf3* knockdown AML12 cells (Fig. 2d). Meanwhile, OXA upregulated the nuclear translocation of *Irf3*, which indicated that IRF3 functions as a transcription factor and can bind to *Ythdf2* in the nucleus to enhance the transcription of *Ythdf2* (Fig. 2e). Additionally, the two binding sites in the promoter regions of *Ythdf2* were predicted using JASPAR (http://jaspar.genereg.net) (Supplementary Fig. 2g). The results of the luciferase reporter assay demonstrated that overexpressing IRF3 upregulated the activity of *Ythdf2* promoter (Fig. 2f) and silencing IRF3 downregulated the activity of *Ythdf2* promoter (Supplementary Fig. 2h). Transferred with *Ythdf2* promoter plasmids which contained mutated IRF3 binding site in AML12 cells could downregulate the activity of *Ythdf2* promoter compared to wild type *Ythdf2* promoter plasmids (Supplementary Fig. 2i). Moreover, we observed that OXA and DMXAA upregulated the activity of *Ythdf2* promoter, whereas SN-011 downregulated the activities of *Ythdf2* promoter in AML12 cells (Fig. 2g). Chromatin immunoprecipitation (ChIP)-qRT-PCR analysis revealed that the enrichment of IRF3 in the *Ythdf2* promoter was significantly higher than that of IgG control in IRF3-overexpressing AML12 cells (Fig. 2h). Additionally, silencing IRF3 in AML12 cells downregulated the enrichment of *Ythdf2* promoter (Supplementary Fig. 2j). OXA and DMXAA upregulated the enrichment of *Ythdf2* promoter, whereas SN-011 downregulated the enrichment of *Ythdf2* promoter in AML12 cells (Fig. 2i). These finding suggested that OXA specifically regulates YTHDF2 expression in hepatocytes through the cGAS-STING-IRF3 signaling pathway. However, OXA did not regulate YTHDF2 expression in tumor cells (Hepa1-6 and MC38 cells) (Supplementary Fig. 2k), $CD8^+$ T cells and macrophages (Supplementary Fig. 2l), indicating that OXA upregulates YTHDF2 expression in hepatocytes rather than the tumor cells and immune cells in the liver microenvironment.

YTHDF2 deficient hepatocytes promote liver tumor growth under OXA stress conditions by impairing $CD8^+$ T cell antitumor response

The role of YTHDF2 in hepatocytes during liver tumor development and chemotherapy treatment was examined using a liver-specific *Ythdf2* KO mouse strain ($Ythdf2^{LKO}$, Supplementary Fig. 3a–b). On day 14 post-orthotopic liver injection of Hepa1-6 (mouse hepatoma cell line) or intrasplenic injection of MC38 (mouse colorectal cancer cell line) into $Ythdf2^{F/F}$ and $Ythdf2^{LKO}$ littermates (Supplementary Fig. 3c–d), the hepatic tumor burden (defined as total liver weight/body weight ratio) in $Ythdf2^{LKO}$ mice was non-significantly higher than that in $Ythdf2^{F/F}$ mice (Supplementary Fig. 3e–f). However, after OXA prestimulation, the tumor burden in $Ythdf2^{LKO}$ mice was significantly higher than that in $Ythdf2^{F/F}$ mice (Fig. 3a–b and Supplementary Fig. 3g–i). These results indicated that YTHDF2 deficiency in hepatocytes reprograms the OXA-exposed liver into a tumor-supporting ecosystem.

Next, the peritumoral tissues of $Ythdf2^{F/F}$ and $Ythdf2^{LKO}$ mice pretreated with OXA and orthotopically injected with Hepa1-6 cells were subjected to RNA sequencing. Deficiency of YTHDF2 dysregulated the expression of several genes (96 upregulated genes and 560 downregulated genes) (Fig. 3c). Gene Ontology (GO) analysis revealed the enrichment of immune-related gene sets (Fig. 3d). Therefore, the immune cell populations in the liver were profiled after sequential OXA pretreatment and tumor inoculation using flow cytometry (Supplementary Fig. 3j). As shown in Fig. 3e and Supplementary Fig. 3k, the percentage and absolute number of $CD8^+$ T cells in $Ythdf2^{LKO}$ mice were significantly lower than those in $Ythdf2^{F/F}$ mice. Additionally, we noticed a profound decrease in the percentage and absolute number of $CD8^+$ TILs from $Ythdf2^{LKO}$ mice. Further, we explored the changes of functional markers and observed lower percentages of tumor-infiltrating $IFN\gamma^+$, $TNF\alpha^+$, $GzmB^+$ $CD8^+$ T cells (Fig. 3f and Supplementary Fig. 3l), and higher percentages of $TIM3^+$ $PD1^+$ $CD8^+$ T cells (Fig. 3f) in the liver of $Ythdf2^{LKO}$ mice, which was consistent with the enhanced tumor burden. Moreover, the decreased antitumor response in $Ythdf2^{LKO}$ mice was completely eliminated when mice received an intraperitoneal (i.p.) injection of CD8 antibody, which induced systemic depletion of $CD8^+$ T cells (Fig. 3g–h and Supplementary Fig. 3m–n). Additionally, the composition and frequency of naïve immune cells in the liver and spleen were similar in age-matched and sex-matched

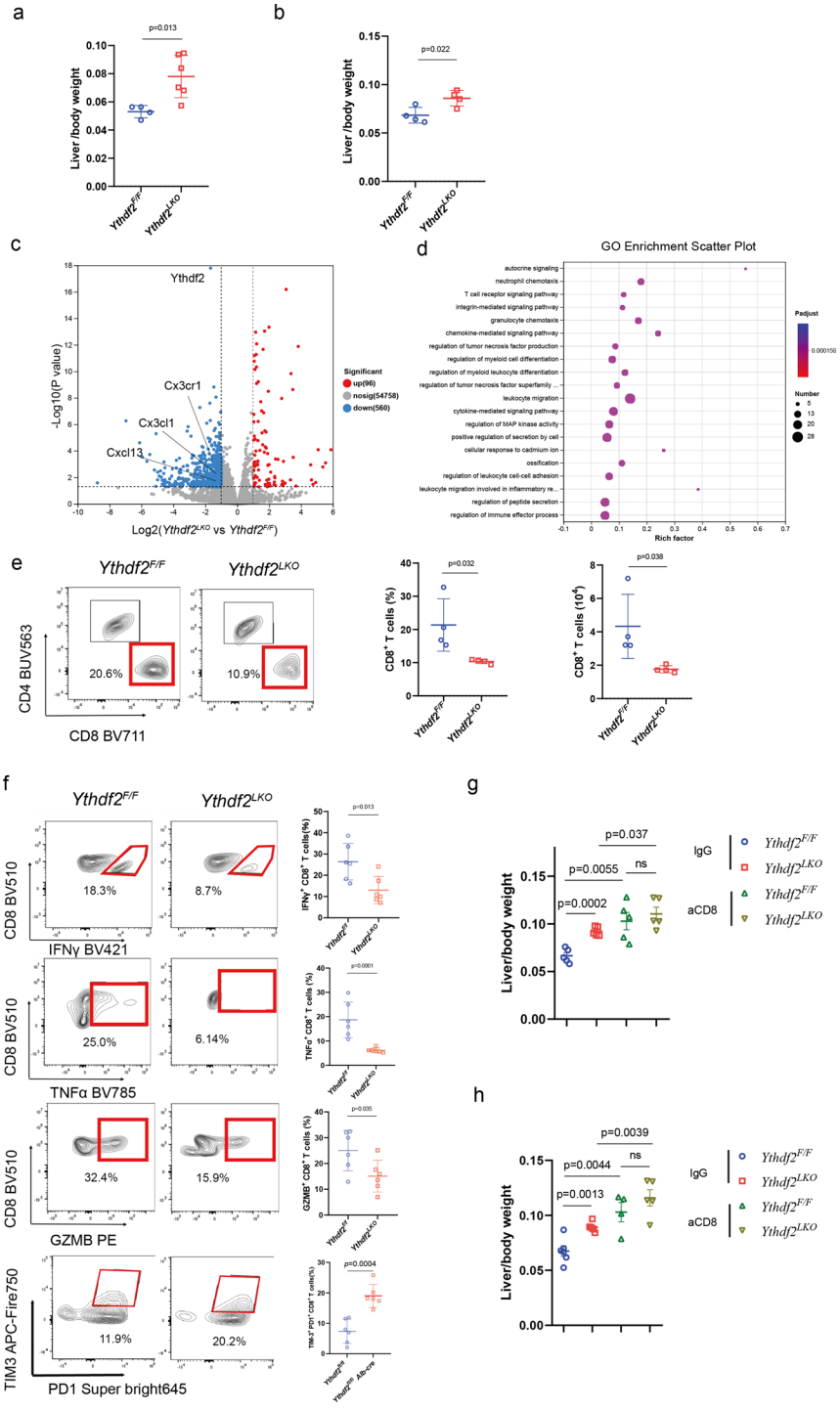

Fig. 3 YTHDF2 deficient hepatocytes promote liver tumor growth under OXA stress conditions by impairing $CD8^+$ T cell antitumor response. **a**,**b**, liver/body weight from *Ythdf2*$^{F/F}$ and *Ythdf2*^{LKO} mice after OXA pre-treatment and Hepa1-6 orthotopic injection (a) or MC38 intrasplenic injection (b)($n = 4$–6). **c**, Volcano plots showing up (red) - or down (blue) -regulated genes in peritumoral tissues from *Ythdf2*$^{F/F}$ versus *Ythdf2*^{LKO} mice after Hepa1-6 orthotopic injection, as assessed by RNA-seq ($n = 3$). **d**, GO analysis based on the RNA-seq in (c), showing the most significant enriched pathways and the P-values. **e**, Representative plots, percentages and absolute numbers of $CD8^+$ T cells from *Ythdf2*$^{F/F}$*and Ythdf2*^{LKO} mice on day 7 after Hepa1-6 orthotopic injection ($n = 4$). **f**, Representative plots and percentages of $IFN\gamma^+$,$TNF\alpha^+$,$GzmB^+$ and $TIM3^+PD1^+$ $CD8^+$ T cells from *Ythdf2*$^{F/F}$ and *Ythdf2*^{LKO} mice on day 7 after Hepa1-6 orthotopic injection ($n = 6$). **g**,**h**, liver/body weight from *Ythdf2*$^{F/F}$ and *Ythdf2*^{LKO} mice treated with IgG/CD8 antibody after Hepa1-6 orthotopic injection (**g**) or MC38 intrasplenic injection (**h**) ($n = 4$–6). Error bars indicate means ± SD. P-values were determined by an unpaired two-tailed t-test (**a**, **b**,**e**-**h**). Data in a-h are representative of at least two independent experiments

Ythdf2$^{F/F}$ and *Ythdf2*^{LKO} mice (Supplementary Fig. 4a–b). Furthermore, *Ythdf2*$^{F/F}$ and *Ythdf2*^{LKO} mice exhibited similar percentages and absolute numbers of tumor-infiltrating B cells, natural killer cells, γδ T cells, CD4$^+$ T cells, macrophages, neutrophils, monocytes, and DCs (Supplementary Fig. 4c–r). Additionally, we evaluated the T cell inflamed gene expression profile by qPCR in tumor tissues from *Ythdf2*$^{F/F}$ and *Ythdf2*^{LKO} mice and observed that the expression of most genes was reduced in *Ythdf2*^{LKO} mice(Supplementary Fig. 4s). These results indicate that hepatic YTHDF2 preserves the immune balance of the liver microenvironment and that the downregulation of YTHDF2 in hepatocytes results in CD8$^+$ T cell dysfunction. Thus, YTHDF2 deficiency in hepatocytes promotes liver tumor growth after chemotherapy in a CD8$^+$ T cell-dependent manner.

YTHDF2 maintains CD8+ T cell-mediated antitumor response through CX3CL1 in hepatocytes

Next, the intrinsic mechanisms involved in hepaticYTHDF2-mediated regulation of CD8$^+$ T cells were examined. GO (Fig. 3d) and Kyoto Encyclopedia of Genes and Genomes (KEGG) analysis (Fig. 4a) of RNA sequencing data of peritumoral tissues after orthotopic tumor inoculation revealed the enrichment of chemokine signaling pathway and cytokine-cytokine receptor interaction in the liver of *Ythdf2*^{LKO} mice. Hepatocytes regulate CD8$^+$ T cell proportion and function indirectly by secreting certain substances or through direct contact. As the chemokine signaling and cytokine-cytokine receptor interaction pathways were downregulated in the liver of *Ythdf2*^{LKO} mice, some cytokines originating from hepatocytes were hypothesized to modulate CD8$^+$ T cells. The serum samples of *Ythdf2*$^{F/F}$ and *Ythdf2*^{LKO} mice were subjected to inflammation antibody array analysis after orthotopic injection of Hepa1-6 cells to identify the potential cytokines that modulate CD8$^+$ T cells (Supplementary Fig. 5a). As shown in Fig. 4b, YTHDF2 deficiency dysregulated the expression of several cytokines (3 upregulated cytokines and 18 downregulated cytokines). Additionally, a combined screening approach was employed by integrating RNA-seq and inflammation antibody array data to identify the key determinants. Transcriptomic and proteomic data demonstrated that YTHDF2 deficiency significantly downregulated the levels of CX3CL1 and CXCL13, which mediate chemoattraction of CD8$^+$ T cells (Fig. 4c). Previous studies have reported that CX3CL1 and CXCL13 are associated with the recruitment and activation of CD8$^+$ T cells [28, 29]. CX3CR1$^+$CD8$^+$ T cells, which exhibit chemoattraction to CX3CL1, were associated with enhanced cytotoxicity and migration and exhibited approximately 10% overlap of T cell receptor clonotypes with CD8$^+$ T cells infiltrating the TME [30]. Hepatic CX3CL1 downregulation in *Ythdf2*^{LKO} mice was validated using qRT-PCR (Fig. 4d), immunoblotting (Supplementary Fig. 5b) analysis of peritumoral tissues and enzyme-linked immunosorbent assay (ELISA) of mice serum (Fig. 4e) after orthotopic tumor inoculation. In contrast, the expression of CXCL13 was not affected (Fig. 4f). Primary hepatocytes (PHCs) of *Ythdf2*$^{F/F}$ and *Ythdf2*^{LKO} mice were detached from fresh liver. The expression of CX3CL1 was downregulated in PHCs of *Ythdf2*^{LKO} mice (Fig. 4g). Additionally, *Ythdf2* was knocked down in the mouse hepatocyte cell line AML12 (Supplementary Fig. 5c-d). The expression of CX3CL1 was downregulated in *Ythdf2* knockdown (KD) AML12 cells (Supplementary Fig. 5e). The expression of CXCL13 was not changed rather in PHCs (Supplementary Fig. 5f) or AML12 (Supplementary Fig. 5g) cells. Flow cytometric analysis of liver TILs after tumor inoculation revealed that the percentage of CX3CR1$^+$ CD8$^+$ T cells in *Ythdf2*$^{F/F}$ mice was higher than that in *Ythdf2*^{LKO} mice (Fig. 4h–i). Next, this study examined if the functions of YTHDF2 in the liver are dependent on CX3CL1. Animal experiments (Supplementary Fig. 5h) were performed by specifically overexpressing CX3CL1 in hepatocytes using the adeno-associated virus (AAV) delivery system. CX3CL1 overexpression suppressed Ythdf2 KO-mediated accelerated tumor progression (Fig. 4j and Supplementary Fig. 5i). The efficacy of AVV delivery system was verified in Supplementary Fig. 5j-k. The percentage and function of CD8$^+$ T cells were not significantly different between *Ythdf2*$^{F/F}$ and *Ythdf2*^{LKO} mice after CX3CL1 overexpression (Fig. 4k–l). Additionally, We evaluated the T cell inflamed gene expression profile by qRT-PCR in tumor tissues from *Ythdf2*$^{F/F}$ and *Ythdf2*^{LKO} mice following the overexpression of CX3CL1 and observed that the expression of most genes was comparable in *Ythdf2*$^{F/F}$ and *Ythdf2*^{LKO} mice (Supplementary Fig. 5l). Furthermore, qRT-PCR analysis (Supplementary Fig. 5m) and ELISA (Supplementary Fig. 5n) revealed that in the liver microenvironment, CX3CL1 was primarily upregulated in the hepatocytes rather than tumor cells or other immune cells.

As the YTHDF2-CX3CL1 axis is essential for CD8$^+$ T cell recruitment and function in *vivo*, the regulatory effects of the YTHDF2-CX3CL1 axis on CD8$^+$ T cells were examined in vitro. PHCs of *Ythdf2*$^{F/F}$ and *Ythdf2*^{LKO} mice were detached from fresh liver and co-cultured with CD8$^+$ T cells from C57BL/6 mouse spleen (separated by a 5-μm membrane) for 12 h (Fig. 5a). The transwell assay results revealed that the migration of CD8$^+$ T cells was suppressed toward PHCs of *Ythdf2*^{LKO} mice (Fig. 5b). CD8$^+$ T cells co-cultured with PHCs of *Ythdf2*$^{F/F}$ and *Ythdf2*^{LKO} mice for 24 h were harvested for flow cytometry analysis. Additionally, CD8$^+$ T cells were co-cultured with Hepa1-6 cells for 24 h to examine the immune functions of CD8 + T cells. The cytotoxicity of CD8$^+$ T cells

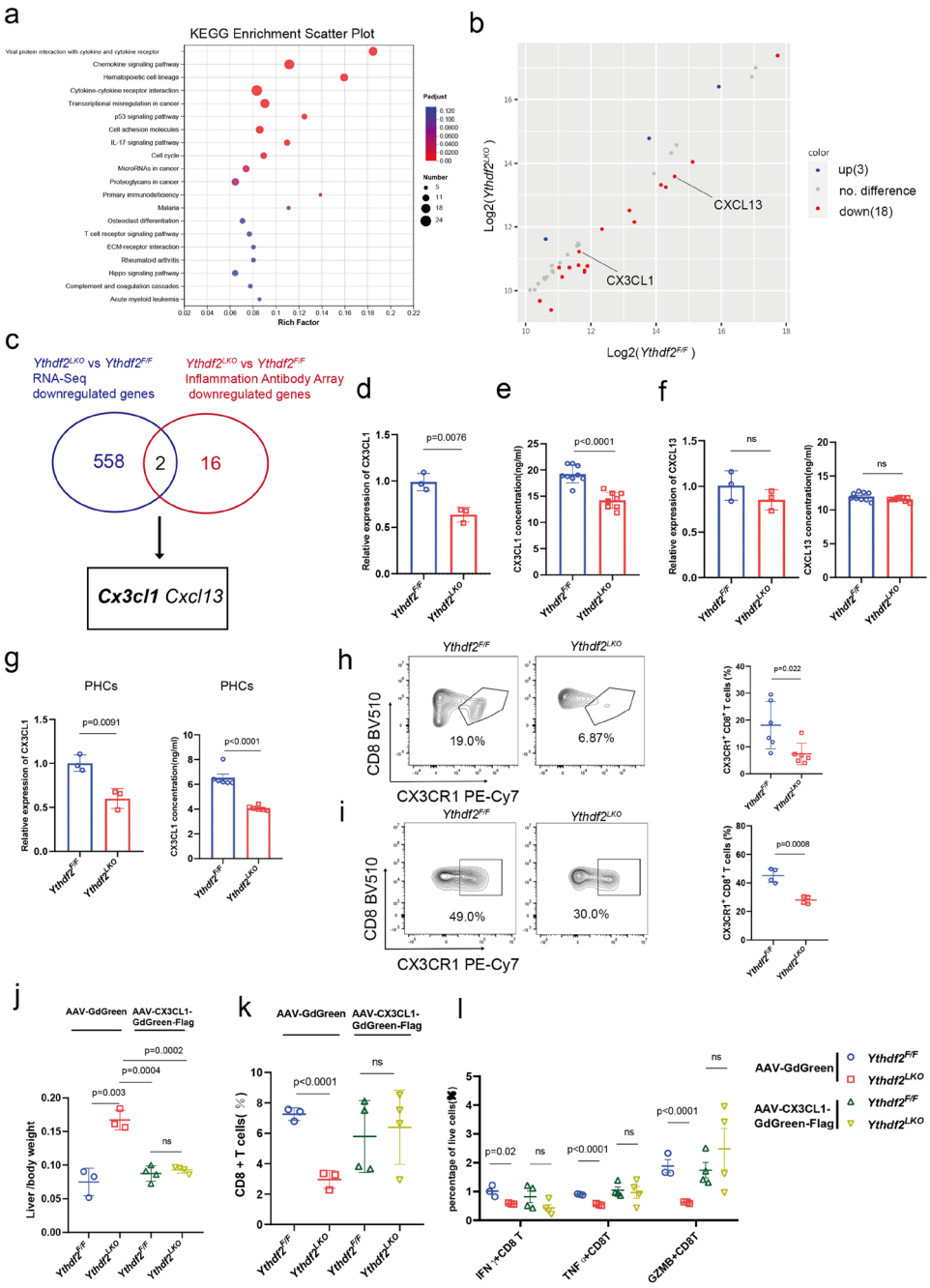

Fig. 4 YTHDF2 maintains CD8$^+$ T cell-mediated antitumor response through CX3CL1 in hepatocytes. **a**, KEGG analysis based on the RNA-seq in peritumoral tissues from *Ythdf2*$^{F/F}$ versus *Ythdf2*^{LKO} mice after Hepa1-6 orthotopic injection, showing the most significant enriched pathways and the P-values. **b**, Volcano plots showing up (red) - or down (blue) -regulated genes in serum from *Ythdf2*$^{F/F}$ versus *Ythdf2*^{LKO} mice after Hepa1-6 orthotopic injection, as assessed by inflammation antibody array ($n = 3$). **c**, Screening strategy showing a group of genes that were concomitant in RNA-seq and inflammation antibody array. **d**, qRT-PCR analysis of the relative mRNA levels of CX3CL1 in peritumoral hepatocytes from *Ythdf2*$^{F/F}$ and *Ythdf2*^{LKO} ($n = 3$). **e**, ELISA analysis of the quantitative protein levels of CX3CL1 in the serum from *Ythdf2*$^{F/F}$ and *Ythdf2*^{LKO} mice ($n = 9$). **f**, qRT-PCR analysis (left) of the relative mRNA levels of CXCL13 in peritumoral hepatocytes from *Ythdf2*$^{F/F}$ and *Ythdf2*^{LKO} ($n = 3$) and ELISA analysis (right) of the quantitative protein levels of CXCL13 in the serum from *Ythdf2*$^{F/F}$ and *Ythdf2*^{LKO} mice ($n = 9$). **g**, qRT-PCR analysis (left, $n = 3$) and ELISA analysis (right, $n = 6$) of CX3CL1 in the PHCs from *Ythdf2*$^{F/F}$ and *Ythdf2*^{LKO} mice. **h**, **i** Representative plots, percentages of CX3CR1$^+$ CD8$^+$ T cells from *Ythdf2*$^{F/F}$*and Ythdf2*^{LKO} mice on day 7 after Hepa1-6 orthotopic injection (h, $n = 6$) and MC38 intrasplenic injection (i, $n = 4$). **j-l** liver/body weight (j), percentages of CD8$^+$ T cells (k), IFNγ$^+$, TNFα$^+$ and GzmB$^+$ CD8$^+$ T cells (l), from *Ythdf2*$^{F/F}$ and *Ythdf2*^{LKO} mice treated with AAV-GdGreen or AAV-CX3CL1-GdGreen-Flag after MC38 intrasplenic injection ($n = 3$–4). Error bars indicate means ± SD. P-values were determined by an unpaired two-tailed t-test (d-l). Data in d-l are representative of at least two independent experiments. ns, not significant

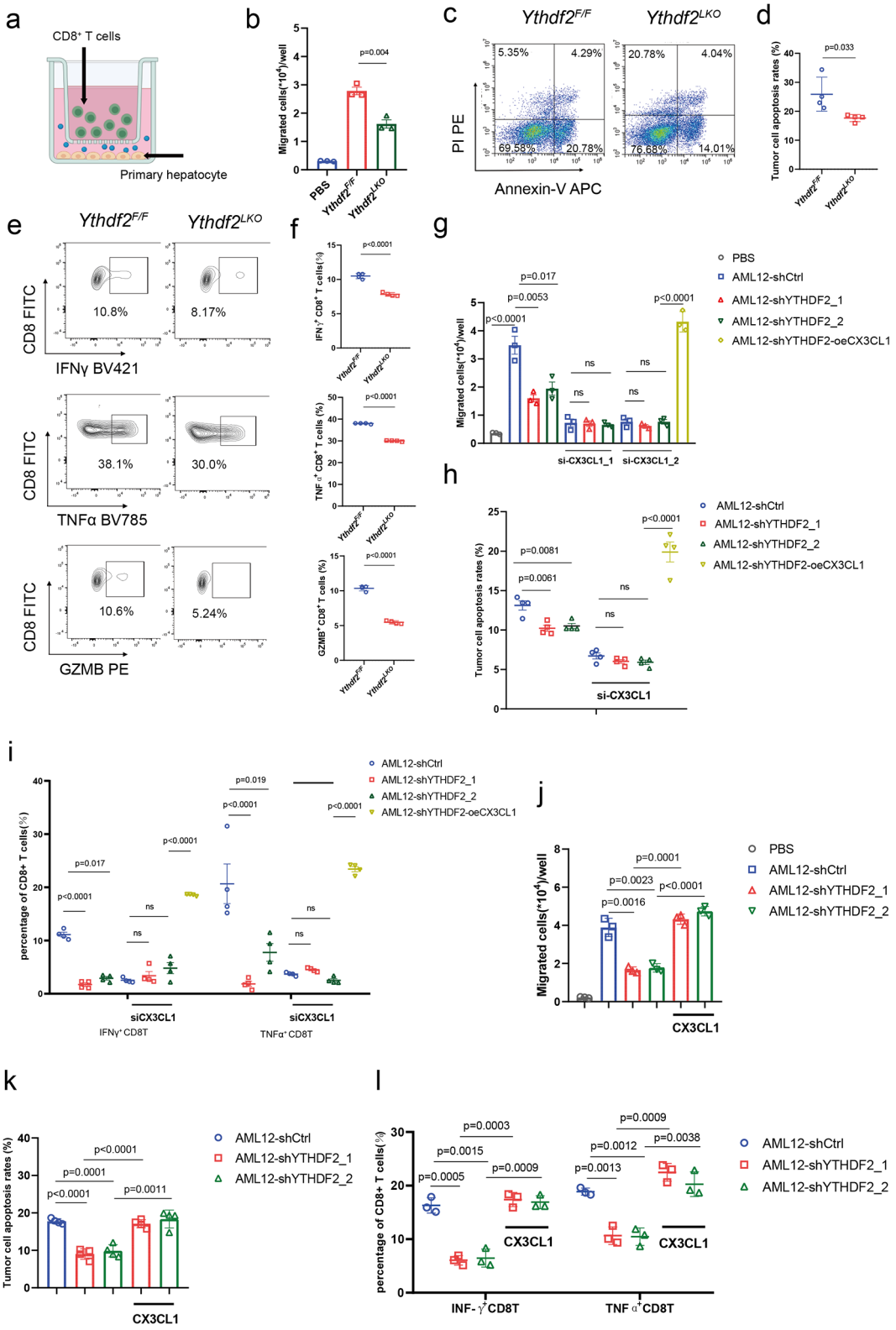

Fig. 5 (See legend on next page.)

(See figure on previous page.)

Fig. 5 YTHDF2-CX3CL1 axis in hepatocytes enhances $CD8^+$ T cells antitumor response *in vitro*. **a**, Illustration of transwell co-culture system for $CD8^+$ T cells and primary hepatocytes. **b**, Chemoattractant effect of primary hepatocytes from *Ythdf2*$^{F/F}$ and *Ythdf2*^{LKO} mice to $CD8^+$ T cells ($n=3$). **c**, **d**, Representative plots (c) and apoptosis rate of Hepa1-6 (d) co-culture with $CD8^+$ T cells from C57BL/6 mice spleen after co-culture with primary hepatocytes from *Ythdf2*$^{F/F}$ and *Ythdf2*^{LKO} mice ($n=4$) (d). **e**, **f**, Representative plots (e) and percentage of $IFN\gamma^+$,$TNF\alpha^+$ and $GzmB^+$ $CD8^+$ T cells (f) from C57BL/6 mice spleen after co-culture with primary hepatocytes from *Ythdf2*$^{F/F}$ and *Ythdf2*^{LKO} mice ($n=4$). **g**, Chemoattractant effect of AML12-Ctrl, AML12-shYTHDF2_1, AML12-shYTHDF2_2, AML12-shYTHDF2-oeCX3CL1, AML12-shCtrl-siCX3CL1, AML12-shYTHDF2_1-siCX3CL1 and AML12-shYTHDF2_2-siCX3CL1 cells to $CD8^+$ T cells ($n=3$). **h**, Apoptosis rate of Hepa1-6 after co-cultured with $CD8^+$ T cells from C57BL/6 mice spleen, which had been co-cultured with AML12-Ctrl, AML12-shYTHDF2_1, AML12-shYTHDF2_2, AML12-shYTHDF2-oeCX3CL1, AML12-shCtrl-siCX3CL1, AML12-shYTHDF2_1-siCX3CL1 and AML12-shYTHDF2_2-siCX3CL1 cells for 24 h ($n=4$). **i**, Percentage of $IFN\gamma^+$ (j), $TNF\alpha^+$ (k) $CD8^+$ T cells from C57BL/6 mice splenic $CD8^+$ T cells which had been co-cultured with AML12-Ctrl, AML12-shYTHDF2_1, AML12-shYTHDF2_2, AML12-shYTHDF2-oeCX3CL1, AML12-shCtrl-siCX3CL1, AML12-shYTHDF2_1-siCX3CL1 and AML12-shYTHDF2_2-siCX3CL1 cells for 24 h ($n=4$). **j**, Chemoattractant effect to $CD8^+$ T cells of AML12-Ctrl, AML12-shYTHDF2_1, AML12-shYTHDF2_2 as well as AML12-shYTHDF2_1, AML12-shYTHDF2_2 which supplemented CX3CL1 ($n=3$). **k**, Apoptosis rate of Hepa1-6 after co-cultured with $CD8^+$ T cells from C57BL/6 mice spleen, which had been co-cultured with AML12-Ctrl, AML12-shYTHDF2_1, AML12-shYTHDF2_2 as well as AML12-shYTHDF2_1, AML12-shYTHDF2_2 which supplemented CX3CL1 for 24 h ($n=4$). **l**, Percentage of $IFN\gamma^+$, $TNF\alpha^+$ $CD8^+$ T cells from C57BL/6 mice splenic $CD8^+$ T cells which had been co-cultured with AML12-Ctrl, AML12-shYTHDF2_1, AML12-shYTHDF2_2 as well as AML12-shYTHDF2_1, AML12-shYTHDF2_2 which supplemented CX3CL1 for 24 h ($n=3$). Error bars indicate means ± SD. P-values were determined by an unpaired two-tailed t-test (b, d,f, g-l). Data in b-l are representative of at least two independent experiments. ns, not significant

was impaired under the education of YTHDF2-depleted PHCs compared with control cells as evidenced by the levels of cytotoxicity-related markers (Fig. 5c–f). Control and *Ythdf2* KD AML12 cells were co-cultured with $CD8^+$ T cells in the transwell system and co-culture system described above. *Ythdf2* KD AML12 cells decreased the recruitment of $CD8^+$ T cells and impaired the cytotoxic function of $CD8^+$ T cells (Fig. 5g–i).

Next, CX3CL1 was overexpressed or knocked down in AML12 cells to examine if the effect of YTHDF2 on $CD8^+$ T cells was dependent on CX3CL1 (Supplementary Fig. 6a–e). The phenomena that lack of YTHDF2 in AML12 cells reduced T cell cytotoxicity and migration was eliminated after silencing CX3CL1, as both YTHDF2 knockdown and control AML12 cells showed impaired ability of inducing T cell activation and recruitment, again addressing the critical role of CX3CL1 (Fig. 5g–i and Supplementary Fig. 6f–h). Furthermore, CX3CL1 overexpression in *Ythdf2* KD AML12 cells upregulated T cell activation and recruitment (Fig. 5g–i and Supplementary Fig. 6f–h). Recombinant mouse CX3CL1 supplementation in the conditioned media rescued the impaired ability of *Ythdf2* KD AML12 cells to activate and recruit T cells (Fig. 5j–l and Supplementary Fig. 6i–k). These results indicate that the YTHDF2-CX3CL1 axis in hepatocytes promotes $CD8^+$ T cell-mediated antitumor response.

Hepatocyte YTHDF2 suppresses liver tumor growth by enhancing *Cx3cl1* mRNA stability in an m^6 A-dependent manner

YTHDF2, an m^6A reader, recognizes the m^6A modifications to regulate the stability and translation status of methylated mRNA [17]. To investigate if YTHDF2 regulates the stability of *Cx3cl1* transcripts, AML12 cells treated with actinomycin D were subjected to mRNA stability profiling. The median half-life of *Cx3cl1* mRNA was shortened in *Ythdf2* KD cells (Fig. 6a) but prolonged in YTHDF2-overexpressing cells (Fig. 6b). YTHDF2 recognizes the m^6A modifications on RNA through the W432 site within the hydrophobic pocket of the YTH domain [31]. To further confirm if YTHDF2-mediated *Cx3cl1* degradation is dependent on the YTH domain and its specific m^6A-binding ability, the YTHDF2^{W432A} mutant-expressing AML12 cells were established (Supplementary Fig. 7a). The median half-life of *Cx3cl1* mRNA in YTHDF2^{W432A} (m^6A recognition-defective mutant)-expressing cells was lower than that in wild-type YTHDF2-expressing cells (Fig. 6b). Additionally, RNA immunoprecipitation (RIP) analysis revealed that YTHDF2^{W432A} could not recognize and bind *Cx3cl1* mRNA when compared with WT YTHDF2 (Fig. 6c). The abundance of m^6A modification at the *Cx3cl1* 3′-untranslated region (UTR) was high. The results of the luciferase reporter assay revealed that slicence of YTHDF2 reduced the activeties of *Cx3cl1* 3′-UTR (Fig. 6d), and WT YTHDF2, but not YTHDF2^{W432A} mutant, increased the activities of *Cx3cl1* 3′-UTR (Supplementary Fig. 7b). Additionally, YTHDF2 did not bind to the promoter region of *Cx3cl1* (Supplementary Fig. 7c–d). These results suggest that YTHDF2 in hepatocytes preserved the stability of *Cx3cl1* mRNA in an m^6A-dependent manner.

Next, vector control-transfected, WT YTHDF2 overexpression construct-transfected, and mutant YTHDF2 overexpression-transfected AML12 cells (Supplementary Fig. 7a) and PHCs from *Ythdf2*^{LKO} mice (Supplementary Fig. 7e) were co-cultured with $CD8^+$ T cells in the transwell system and co-culture system described above. WT YTHDF2-overexpressing AML12 cells, but not mutant YTHDF2-overexpressing AML12 cells, increased the migration (Fig. 6e) and cytotoxic effects (Fig. 6g-i) of $CD8^+$ T cells. Similarly, WT YTHDF2-overexpressing PHCs from *Ythdf2*^{LKO} mice increased the migration (Fig. 6j) and cytotoxic effects (Fig. 6k-l and Supplementary Fig. 7f-g) of $CD8^+$ T cells.

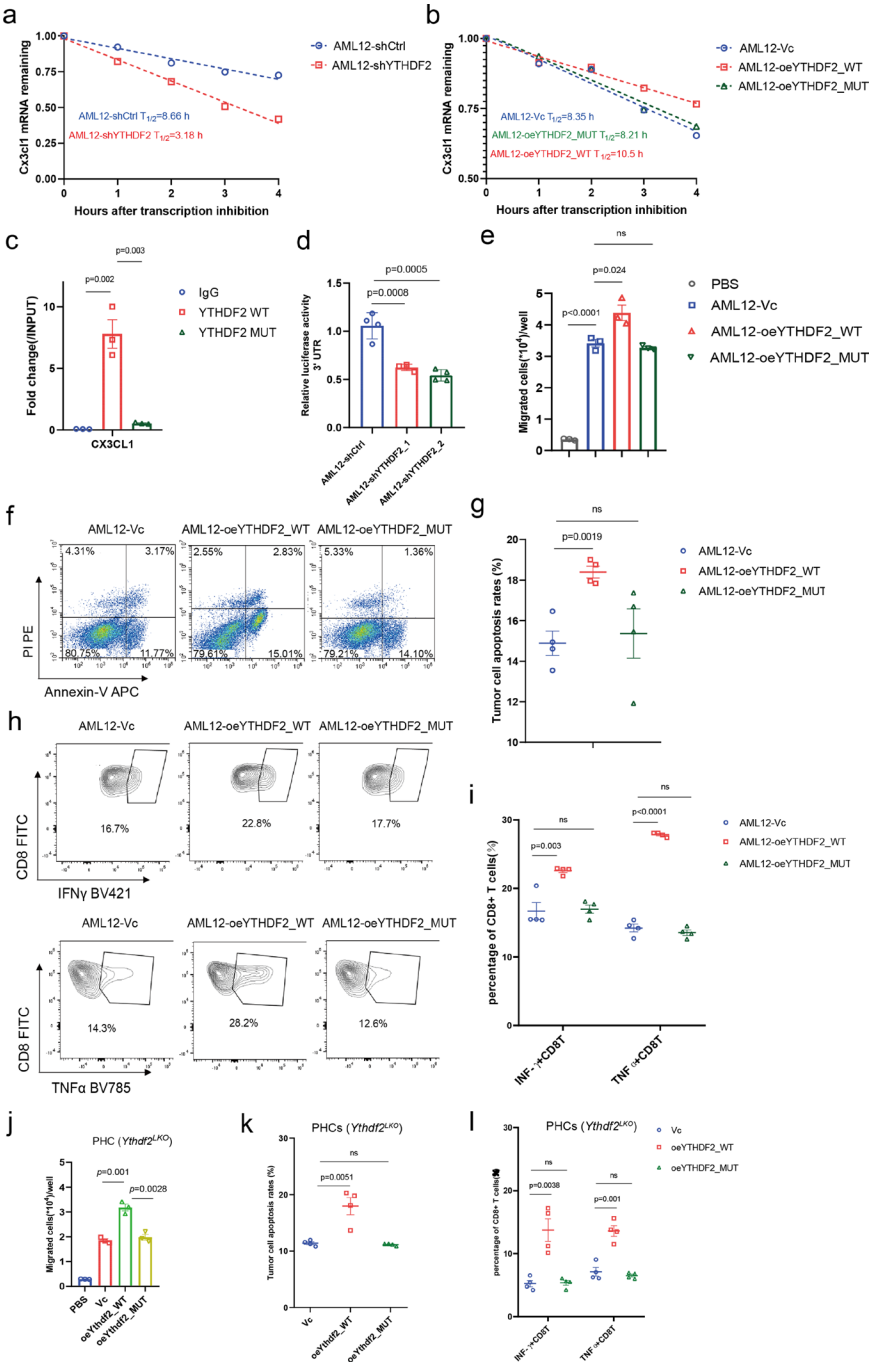

Fig. 6 Hepatocyte YTHDF2 suppresses liver tumor growth by enhancing *Cx3cl1* mRNA stability in an m^{6}A-dependent manner. **a**, **b**, Lifetime of CX3CL1 mRNA in AML12-shCtrl and AML12-shYTHDF2 cells (a), AML12-vc, AML12-oeYTHDF2_WT and AML12-oeYTHDF2_MUT cells (b). Transcription was inhibited by actinomycin D (5 μg/mL) ($n=3$). **c**, RIP-qPCR showed the interaction of CX3CL1 transcripts with YTHDF2 in AML12-Vc, AML12-oeYTHDF2_WT and AML12-oeYTHDF2_MUT cells ($n=3$). **d**, Relative luciferase activity of constructs containing 3'UTR of CX3CL1 in AML12-Ctrl, AML12-shYTHDF2_1 and AML12-shYTHDF2_2 cells ($n=4$). **e**, Chemoattractant effect of AML12-vc, AML12-oeYTHDF2_WT and AML12-oeYTHDF2_MUT cells to CD8$^+$ T cells ($n=3$). **f**, **g**, Representative plots (f) and apoptosis rate of Hepa1-6 (g) co-culture with CD8$^+$ T cells from C57BL/6 mice spleen after co-culture with AML12-vc, AML12-oeYTHDF2_WT and AML12-oeYTHDF2_MUT cells ($n=4$). **h**, **i**, Representative plots (h) and percentage of IFNγ$^+$,TNFα$^+$ CD8$^+$ T cells (i) from C57BL/6 mice spleen after co-culture with AML12-vc, AML12-oeYTHDF2_WT and AML12-oeYTHDF2_MUT cells ($n=4$). **j**, Chemoattractant effect of Vc, oeYTHDF2_WT and oeYTHDF2_MUT of PHCs from *Ythdf2*^{LKO} mice to CD8$^+$ T cells ($n=3$). **k**, Apoptosis rate of Hepa1-6 co-culture with CD8$^+$ T cells from C57BL/6 mice spleen after co-culture with Vc, oeYTHDF2_WT and oeYTHDF2_MUT of PHCs from *Ythdf2*^{LKO} mice ($n=4$). **l**, Percentage of IFNγ$^+$,TNFα$^+$ CD8$^+$ T cells from C57BL/6 mice spleen after co-culture with Vc, oeYTHDF2_WT and oeYTHDF2_MUT of PHCs from *Ythdf2*^{LKO} mice ($n=4$).Error bars indicate means ± SD. P-values were determined by an unpaired two-tailed t-test (c-e, g,i-l). Data in a-l are representative of at least two independent experiments. ns, not significant

YTHDF2-CX3CL1 axis in hepatocytes enhances the antitumor efficacy of immunotherapy

The upregulation of CX3CL1 expression and $CD8^+$ T cell infiltration in peritumoral tissues of patients treated with HAIC was validated using immunohistochemical staining (Fig. 7a–d). Correlation analysis revealed that YTHDF2 was positively correlated with CX3CL1(Fig. 7e) and $CD8^+$ T cells (Fig. 7f) in the study cohort. The correlation analysis results of YTHDF2, CX3CL1, and $CD8^+$ T cells were validated using The Cancer Genome Atlas-Liver HCC cohort (Supplementary Fig. 8a–c).

The YTHDF2-CX3CL1 axis in hepatocytes was positively correlated with $CD8^+$ T cells. Hence, this study investigated if the YTHDF2-CX3CL1 axis was associated with the efficacy of immunotherapy. *Ythdf2*$^{F/F}$ mice with liver tumors exhibited resistance to treatment with OXA or anti-PD1 antibody monotherapy (Supplementary Fig. 8d–f). However, the combination of OXA and anti-PD1 antibody (Supplementary Fig. 8g) significantly decreased the tumor burden (Fig. 7g-h). In contrast, the efficacy of the combination therapy was diminished in *Ythdf2*^{LKO} mice, indicating that the synergistic therapeutic effects of chemotherapy and immunotherapy on liver cancer were dependent on hepatic YTHDF2 expression (Fig. 7g–h). We evaluated the infiltration of $CD8^+$ T cells by immunohistological staining, and observed that there were largest number of infiltrated $CD8^+$ T cells in *Ythdf2*$^{F/F}$ mice received combination therapy and less $CD8^+$ T cells in *Ythdf2*^{LKO} mice (Fig. 7i and Supplementary Fig. 8h). YTHDF2 downregulation is a contraindication for chemo-immunotherapy. This may be because YTHDF2 downregulation results in decreased cytotoxic $CD8^+$ T cell infiltration, suppressing the efficacy of PD-1 blockade. Then, the combination of OXA and anti-PD1 antibody were performed after specifically overexpressing CX3CL1 in hepatocytes using the AAV (Supplementary Fig. 8i). The efficacy of the combination therapy was rescued in *Ythdf2*^{LKO} mice after overexpression of CX3CL1(Fig. 7j and Supplementary Fig. 8j). Additionally, YTHDF2 upregulation in peritumoral tissues of patients treated with HAIC and anti-PD1 antibodies was correlated with improved prognostic outcomes (Fig. 7k–l). These findings indicate that the YTHDF2-CX3CL1 axis in hepatocytes enhances the antitumor efficacy of immunotherapy.

Discussion

This study demonstrated that the chemotherapy agent OXA upregulates hepatic YTHDF2 expression by activating the cGAS-STING signaling pathway. The YTHDF2-CX3CL1 axis in hepatocytes regulated the $CD8^+$ T cell-mediated antitumor immune responses in an m^6A-dependent manner, contributing to improved clinical outcomes in patients treated with the combination of immunotherapy and chemotherapy. These findings indicate that the YTHDF2-CX3CL1 axis in hepatocytes is a potential novel therapeutic target for primary and metastatic liver malignancies (Fig. 8).

OXA belongs to the third generation of drugs that specifically target DNA. Previous studies have suggested that RNA m^6A modification plays a pivotal role in mediating the cellular response to short-term ultraviolet (UV) irradiation-induced DNA damage [32]. This study demonstrated that OXA upregulated the mRNA and protein levels of YTHDF2 in hepatocytes by activating the cGAS-STING signaling pathway, indirectly regulating immune responses. This regulatory mechanism appears to be limited to hepatocytes as it was not observed in tumor cells. These findings improved our understanding of the intricate interplay between platinum-based drugs and cellular signaling pathways and established a foundation for the immune sensitization of liver cancer to chemotherapy. Additonally, whether other chemotherapeutic agents and treatment modalities could lead to a similar effect will be an objective of our forthcoming investigation.

TME is a specialized environment in which tumor cells exist and interact with the surrounding non-tumor components. Additionally, the TME is a complex network comprising various cellular and non-cellular elements involved in tumor growth and progression [33, 34]. Peritumoral hepatocytes function as critical components in the liver TME. This study established the *Ythdf2*^{LKO} mouse model, as well as the orthotopic and colon metastatic liver tumor models. Remarkably, our investigations unveil a compelling association wherein the loss of YTHDF2 specifically within hepatocytes engenders a milieu within the liver that profoundly fosters tumorigenic growth, not only in primary hepatic neoplasms but also in the context of metastatic liver tumors. This study, for the first time, elucidated the regulatory effect of paracancerous hepatocytes on the immune microenvironment and demonstrated their unique specificity to the hepatic milieu irrespective of the cancer type. Additionally, these novel findings provide additional insights into the role of hepatocyte YTHDF2 in mediating the intricate dynamics of the hepatic microenvironment.

Chemokines play a crucial role in promoting the migration of immune cells and consequently facilitating the initiation and execution of an efficient antitumor immune response [35]. Previous studies have reported the correlation between CX3CL1 upregulation and an increased abundance of TILs, suggesting the role of this chemotactic factor in facilitating the recruitment of immune cells to the malignant lesion [36]. This study demonstrated that the effect of YTHDF2 on $CD8^+$ T cells is mediated through CX3CL1. Additionally, the supplementation of CX3CL1 effectively restored the YTHDF2 deficiency-induced attenuation of antitumor response

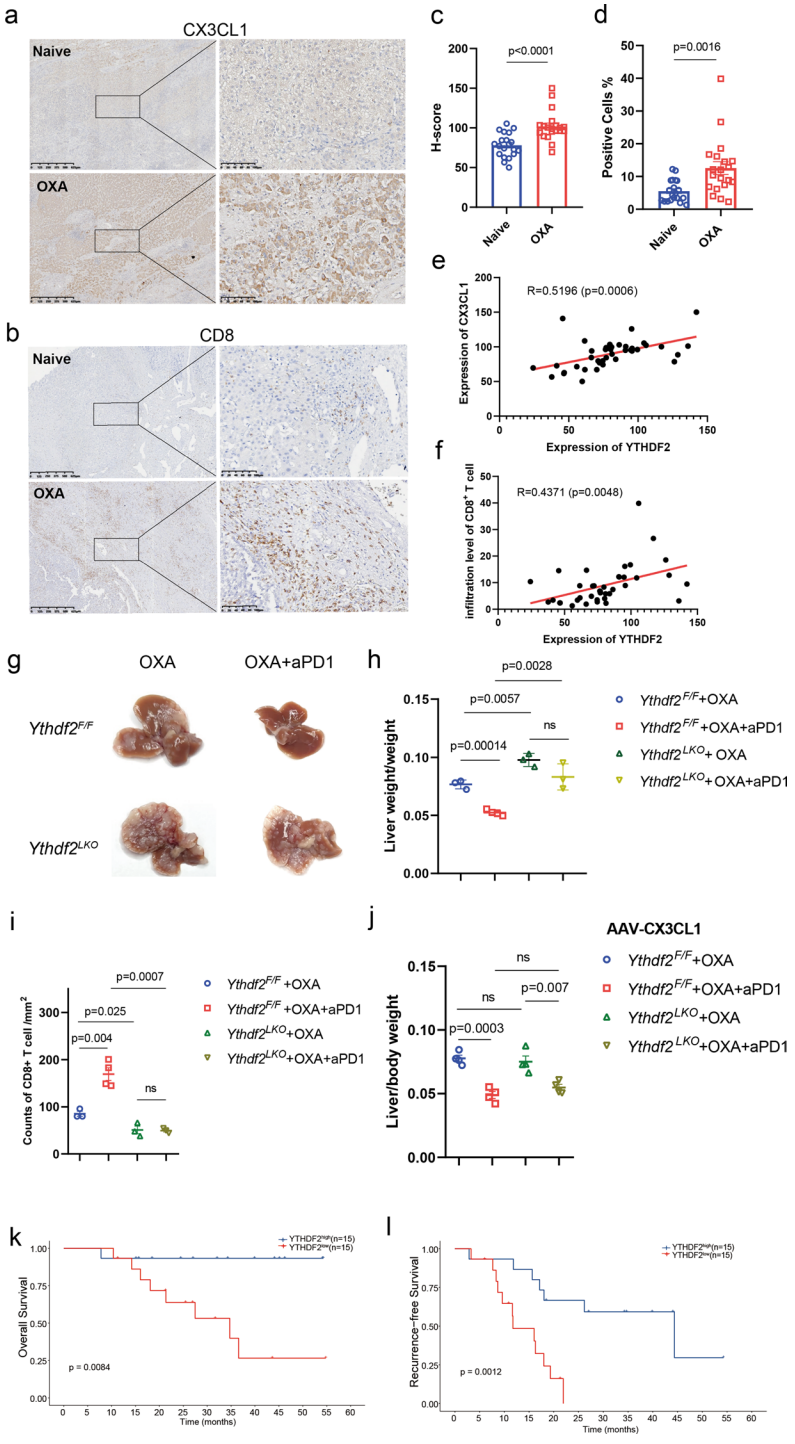

Fig. 7 YTHDF2-CX3CL1 axis in hepatocytes enhances the antitumor efficacy of immunotherapy. **a-d**, Immunohistological staining (a, b), H-SCORE value (c) and percentage of positive cells (d) of CX3CL1 and CD8 in peritumoral tissues from treatment naive HCC patients and HCC patients treated with HAIC ($n=20$). **e**, **f**, Scatter plots showing the correlation between YTHDF2 expression and CX3CL1 expression (e) or infiltration $CD8^+$ T cells level (f). The linear best fit line, Pearson correlation coefficient (R) and P-value are shown ($n=20$). **g**, **h**, Gross appearances of liver samples with tumors (g), liver/ body weight (h), from *Ythdf2*$^{F/F}$ and *Ythdf2*^{LKO} mice after MC38 intrasplenic injection treated with OXA and aPD1 ($n=3$–4). **i**, Counts of $CD8^+$ T cells in tumors from *Ythdf2*$^{F/F}$ and *Ythdf2*^{LKO} mice after MC38 intrasplenic injection treated with OXA and aPD1($n=3$–4). **j**, Liver/ body weight from *Ythdf2*$^{F/F}$ and *Ythdf2*^{LKO} mice which received MC38 intrasplenic injection and treated with OXA and aPD1 after overexpression of CX3CL1 ($n=4$). **k**, **l**, Kaplan-Meier analyses of the correlation between YTHDF2 expression level in pare-tumor tissues and overall survival (k) or recurrence-free survival (l) in patients treated with HAIC combined with aPD1 ($n=30$ in total). Error bars indicate means ± SD. P-values were determined by an unpaired two-tailed t-test (c, d,h-j) or Spearman correlation (e, f). P-values were calculated using the log-rank test (k, l). Data in a-l are representative of at least two independent experiments. ns, not significant

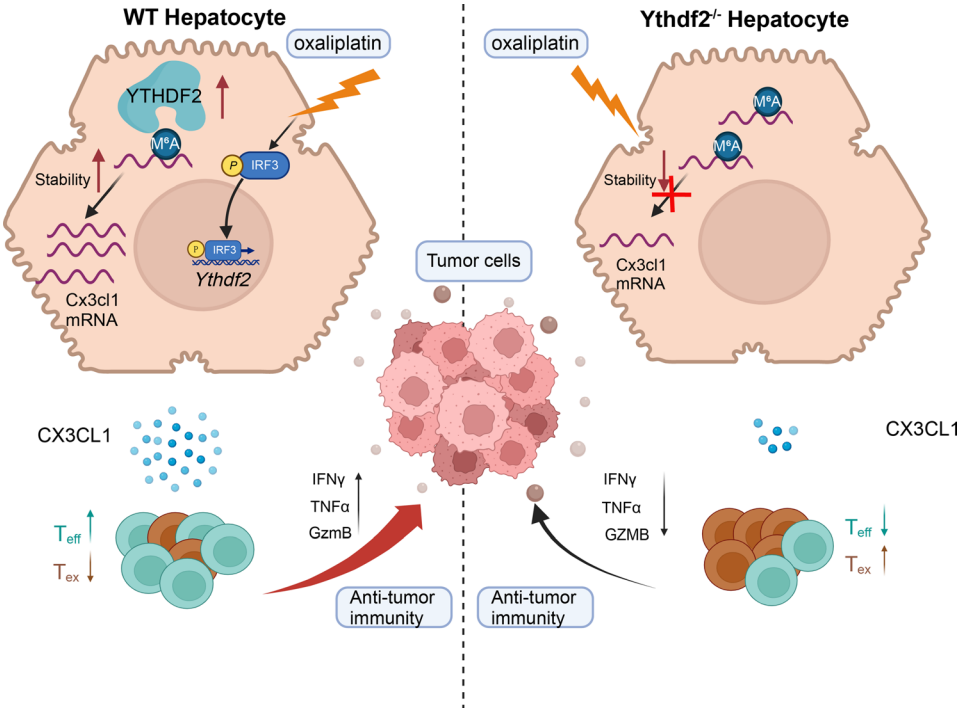

Fig. 8 Schematic depiction of the mechanism underlying how YTHDF2 in peritumoral hepatocytes impedes liver malignances progression and enhances immunotherapy efficacy

in vivo and in vitro. In detail, we observed that overexpression of CX3CL1 in *Ythdf2*^{LKO} mice could rescue the function of CD8$^+$ T cells, and we evaluated the T cell inflamed gene expression profile by qPCR in tumor tissues from *Ythdf2*$^{F/F}$ and *Ythdf2*^{LKO} mice following the overexpression of CX3CL1 and observed that the expression of most genes was comparable. The supplementation of CX3CL1 could recruit and activate the CD8$^+$ T cells. Thus, the YTHDF2-CX3CL1 axis in hepatocytes has a critical role in CD8$^+$ T cell-mediated antitumor immune responses. However, we also observed that in vivo overexpression of CX3CL1 in *Ythdf2*$^{F/F}$ mice could not recruit more CD8 + T cells. It might be explained that due to the existence of immune regulatory network, there must be other pathways to regulate CD8 + T cells and maintain homeostasis. Therefore, additional supplementation of CX3CL1 in *Ythdf2*$^{F/F}$ mice did not further increase the number of CD8 + T cells. Elucidation of the immune network regulated by the YTHDF2-CX3CL1 axis will enable the development of novel immune-based anti-cancer therapeutic strategies, expanding the arsenal of efficacious interventions for malignancies.

YTHDF2, an m^{6}A reader, has dual roles in HCC, revealing the intricate and multifaceted roles of m^{6}A modifications [19, 22, 37–39]. The role of YTHDF2 in promoting RNA degradation has been widely studied. However, recent studies suggest that YTHDF2 also exerts a positive influence on the preservation of m^{6}A-modified RNA. YTHDF2 has been identified as a glioblastoma stem cell-specific effector that exerts a tumor-promoting effect through the stabilization of *MYC* transcripts [40]. Moreover, YTHDF2 promotes cell cycle progression and contributes to hepatitis B virus-related HCC tumorigenesis by stabilizing *MCM2* and *MCM5* transcripts [41]. The findings of this study are consistent with those of previous studies, which reported the non-canonical role of m^{6}A methylation. Comprehensive analysis of RNA-seq data revealed that *Ythdf2* silencing downregulated the levels of various transcripts. These observations suggest a complex interplay between YTHDF2 and the ultimate fate of m^{6}A-modified transcripts, which may be mediated through the modulation of specific regulatory factors in a cell type-specific manner. These diverse roles of YTHDF2 in different cell types or tissues indicate the complex regulatory mechanisms involved in m^{6}A-mediated post-transcriptional gene regulation, which requires further investigation.

There are many factors associated with YTHDF2 modulation according to previous studies. For example, Jianhua Yu etc. observed that IL-10 – STAT3 signaling regulates YTHDF2 expression in tumor associated macrophages [21]. Another study clarified that ionizing radiation could induce the expression of YTHDF2 in myeloid-derived suppressor cell [42]. In HCC, YTHDF2 O-GlcNAcylation was markedly increased upon HBV infection which enhanced its protein stability [41]. In our study, we discovered that OXA upregulated the mRNA and protein levels of YTHDF2 in hepatocytes by

activating the cGAS-STING signaling pathway. In summary, YTHDF2 may be regulated by multiple signaling pathways in different types of cells under distinct pathophysiological conditions.

Several therapeutic strategies have been developed for cancer to address the challenge of effectively treating malignancies. Among these, combination therapy is an emerging therapeutic modality. Clinical studies examining the therapeutic potential of the combination of OXA-based chemotherapy and immunotherapy are currently ongoing [43–45]. This study demonstrated that the antitumor efficacy of the combination of OXA and anti-PD1 antibody therapy was higher than that of OXA or anti-PD1 antibody monotherapy. However, the therapeutic efficacy of the combination of OXA and anti-PD1 antibody was mitigated in *Ythdf2*^{LKO} mice, indicating the critical role of YTHDF2 in determining the efficacy of combination therapy. Furthermore, analysis of peritumoral tissues from patients treated with the combination of HAIC and anti-PD1 antibody revealed that YTHDF2 upregulation was correlated with improved prognostic outcomes. These observations suggest that YTHDF2 expression is a key determinant of the efficacy of OXA and immunotherapy combination, providing a mechanistic basis for the enhanced therapeutic benefit of OXA treatment. Recent studies on RNA modification have highlighted the potential utility of small-molecule inhibitors targeting m6A modifiers, such as METTL3, FTO, and ALKBH5 for cancer therapy [46–48]. Additionally, a recent study demonstrated that targeting YTHDF2 in macrophages using small interfering RNAs (siRNAs) significantly suppressed tumor growth [21]. This study suggested that targeting the YTHDF2-CX3CL1 axis in hepatocytes in combination with immunotherapy is a potential therapeutic strategy for liver cancers.

Methods

Human specimens

The adjacent peritumoral tissues and tumor tissues were obtained from patients with HCC who underwent curative liver resection at the Department of Liver Surgery, Sun Yat-sen University Cancer Center. All specimens were collected after obtaining written informed consent from the patients. The experiments were approved by the institutional review board of Sun Yat-sen University Cancer Center (approval number: B2024-178-01). The tissue microarrays were collected from 103 treatment-naïve patients who were enrolled between 2008 and 2014. The patients were routinely followed up after curative liver resection. The baseline characteristics of the enrolled patients are summarized in Supplementary Table (1) Forty patients with HCC who underwent curative resection after treatment with OXA-based HAIC or were treatment-naïve were enrolled from February 2019 to February 2022. Thirty patients with HCC who underwent curative resection after treatment with the combination of OXA-based HAIC and anti-PD1 antibody were enrolled from February 2019 to February 2022. The baseline characteristics of the enrolled patients are summarized in Supplementary Table (2) A sample of the surgically resected tissues was immediately transferred to liquid nitrogen for RNA or protein extraction. The pathological tissues were processed for histological staining and further analysis.

m6A dot blot analysis

RNA samples were denatured at 65 °C for 5 min in three times the volume of RNA incubation buffer. After adding isopycnic chilled 20× SSC buffer (Sigma-Aldrich), the samples were spotted on the nitrocellulose membrane. The membrane was washed with 1× Tris-buffered saline containing Tween-20 (TBST) buffer after UV crosslinking for 10 min. Next, the membrane was blocked with 5% non-fat milk and incubated with anti-m^{6}A antibodies (Synaptic Systems, 202003, 1:1000) overnight at 4 °C. The membrane was then incubated with horseradish peroxidase (HRP)-conjugated goat anti-rabbit IgG (Cell Signaling Technology, 7074) for 1 h at room temperature. Immunoreactive signals were developed using the Mine Chemi chemiluminescent imaging system (SageCreation, China).

Immunohistochemical analysis

The serial sections of tissues of patients with HCC were subjected to immunohistochemical analysis. The tissue sections were deparaffinized, subjected to antigen retrieval, and incubated with anti-YTHDF2 (Abcam, ab246514), anti-CX3CL1 (Proteintech, 10108-2-AP), and anti-CD8 (Abcam, ab237709; Cell Signaling Technology, 98941) antibodies. Next, the sections were incubated with the rabbit secondary antibodies. Immunoreactive signals were visualized using HRP-conjugated secondary antibodies (Dako, k5007). The stained sections were assessed using the histochemistry score (H-SCORE) algorithm, which was implemented in the HALO software.

qRT-PCR analysis

Total RNA was extracted from tissues and cultured cells using the RNA quick purification kit (EScience, China), following the manufacturer's instructions. The isolated RNA was reverse-transcribed into complementary DNA using the PrimeScript™ RT Master Mix (Takara, Japan), following the manufacturer's instructions. Further, a triplicate qRT-PCR was performed using SYBR Green and a Roche LightCycler 480 Real-Time PCR System. The primers used in qRT-PCR analysis are listed in Supplementary Table 3.

Immunoblotting

Tissues and cultured cells were lysed in radioimmunoprecipitation assay lysis buffer (Thermo Fisher Scientific, Rockford, IL, USA). Equal amounts of proteins were subjected to sodium dodecyl sulfate-polyacrylamide gel electrophoresis. The resolved proteins were electrophoretically transferred to a polyvinylidene membrane. After blocking with 5% non-fat milk in TBST for 1 h at room temperature, the membrane was incubated with anti-YTHDF2 (Abcam, ab220163), anti-phospho-TBK1 (Cell Signaling Technology, 5483), anti-TBK1 (Cell Signaling Technology, 3504), anti-phospho-IRF3 (Cell Signaling Technology, 83611), anti-IRF3 (Cell Signaling Technology, 4302), anti-phospho-STING (Cell Signaling Technology, 72971), anti-STING (Cell Signaling Technology, 13647), anti-Flag (Cell Signaling Technology, 14793), anti-GAPDH (Cell Signaling Technology, 5174), and anti-Lamin B1 (Cell Signaling Technology, 13435) primary antibodies overnight at 4 °C. Next, the membrane was incubated with HRP-conjugated secondary antibodies (1:5000) for 1 h at ambient temperature. Immunoreactive signals were developed using the Mine Chemi chemiluminescent imaging system (SageCreation, China).

Cell lines and culture

The mouse hepatoma cell line Hepa1-6 was obtained from the Cell Bank of the Type Culture Collection of the Chinese Academy of Sciences. The mouse colon adenocarcinoma cell line MC38 was provided by RH, Xu (Sun Yat-sen University Cancer Center). The mouse hepatocyte cell line AML12 was obtained from the Cell Bank of the Type Culture Collection of the Chinese Academy of Sciences. HEK293T cells were purchased from the Cell Bank of the Type Culture Collection of the Chinese Academy of Sciences. AML12 cells were cultured in William's E medium supplemented with 10% fetal bovine serum (FBS) (Gibco) and insulin-transferrin-selenium (100×, Thermo Fisher) at 37 °C and 5% CO_2. Other cell lines were cultured in Dulbecco's modified Eagle medium supplemented with 10% FBS (Gibco) at 37 °C and 5% CO_2.

The cells were incubated with OXA (4 μg/mL, Selleck), SN-011 (10 μM, Selleck), or DMXAA (10 μM, Selleck) for 24 h.

Animal experiments and models

Wild-type C57BL/6 mice were purchased from Beijing Vital River Laboratory Animal.

Technology Co., Ltd. *Ythdf2*$^{F/F}$ mice were purchased from Shanghai Model Organisms Center, Inc. *Alb*^{cre} mice were a kind gift from MS. Zeng (Sun Yat-sen University Cancer Center). *Ythdf2*$^{F/F}$ mice were crossed with *Alb*^{cre} mice to generate *Ythdf2*^{LKO} mice. All mice were maintained under specific pathogen-free conditions in the animal facilities of Sun Yat-sen University Cancer Center. Mice aged 6–12 weeks were used for the experiments. All animal experiments were approved by the Laboratory Animal Ethics Committee of Sun Yat-sen University (approval number: L025501202203019). The following primers were used for genotyping: *Ythdf2*$^{F/F}$ _F: GCTTG CCTGCTACATAGTGAGA, *Ythdf2*$^{F/F}$ _R: AACTGAAC TGCTTAACCTTCTGG; *Alb*^{cre}_F: GAAGCAGAAGCT TAGGAAGATGG, *Alb*^{cre}_R: TTGGCCCCTTACCATA ACTG.

An orthotopic liver tumor model was established by intrahepatically injecting Hepa1-6 cells (1×10^6 cells). Briefly, the mice were anesthetized, and a midline incision was introduced to expose the liver. Hepa1–6 cells in 25 μL Matrigel (Corning, 356231) were injected under the hepatic capsule into the liver. The operative incision was closed with sutures. A liver metastatic tumor model was established through the intrasplenic injection of MC38 cells (1×10^6 cells). Briefly, the mice were anesthetized, and a left subcostal incision was introduced to expose the spleen. MC38 cells in 100 μL phosphate-buffered saline (PBS) were injected into the spleen. The lower part of the spleen was ligated and removed to avoid the growth of tumor cells in the spleen, while the upper part of the spleen was preserved to maintain immune function. The operative incision was closed with sutures. Finally, the mice were sacrificed for postmortem analysis at the indicated time points. The liver weight/body weight ratio was used as a measure of tumor burden. Mice were intraperitoneally injected with OXA (Selleck, 3 mg/kg bodyweight) once every 3 days for two weeks before tumor inoculation. Mice were intraperitoneally injected with 5-Fu (Selleck, 25 mg/kg bodyweight) twice a week for two weeks. For $CD8^+$ T cell depletion, the mice were intraperitoneally injected with 200 μg of anti-CD8 (BioXcell, BE0061) antibodies on days 1 before tumor inoculation and 2, 5, 8, 11 post-tumor inoculation. For therapeutic anti-PD1 treatment, mice were intraperitoneally injected with 150 μg of anti-PD1 antibody (BioXcell, BE0146) once every 3 days for three times. To overexpress CX3CL1 in hepatocytes, mice were intravenously injected with AAV8-TGB-Cx3cl1-GdGreen-Flag (3.0×10^{11} vg/mouse, Obio Technology, China) 3 weeks before tumor inoculation.

Primary mouse hepatocyte isolation

After administering the anesthetic, a U-shaped incision was introduced in the skin, delicately securing the skin near the head using a needle. The vena cava was precisely cannulated. The liver was perfused to clear blood and circulating cells. The samples were incubated with ethylenediaminetetraacetic acid (EDTA) to remove calcium. Subsequently, the liver was infused with collagenase to disassociate the extracellular matrix. The liver

was dissected, and the hepatocytes were obtained using density-based separation.

Flow cytometry

Single-cell suspensions were prepared from fresh spleens and livers of *Ythdf2*$^{F/F}$ and *Ythdf2*^{LKO} mice as described previously [49]. Briefly, the liver tissues were triturated and digested with the mouse liver dissociation kit (Miltenyi) at 37 °C for 1 h. Single-cell suspension was filtered through a 70-μm cell mesh, and the samples were resuspended in PBS with 2% FBS. The spleen was triturated, and the cell suspension was filtered through a 40-μm cell mesh. The samples were resuspended in PBS with 2% FBS. For surface staining, the samples were incubated with the indicated antibodies for 30 min on ice in the dark. Meanwhile, for intracellular staining, cells were fixed with fixation/permeabilization concentrate (Invitrogen) and fixation/perm diluent (Invitrogen) in a ratio of 1:3 for 40 min at 37 °C and washed twice with diluted 1× permeabilization buffer (10×, BioLegend). For cytokine staining, T cells were incubated in a culture medium containing a cell stimulation cocktail (500×, Invitrogen) at 37 °C for 4 h. Next, the cells were incubated with the indicated antibodies for 30 min at 37 °C in the dark. Flow cytometry was performed using Cytek Aurora (CytekBiosciences). The data were analyzed using FlowJo. The fluorescent dye-labeled antibodies, which were purchased from BioLegend, BD Biosciences, or Thermo Fisher, used in this study are summarized in Supplementary Table 4.

Mouse CD8+ T cell isolation and activation

Mouse CD8$^+$ T cells were isolated from the spleen of wild-type mice. The spleen was triturated, and the suspension was filtered through a 40-μm cell mesh. The samples were resuspended in PBS with 2% FBS. CD8$^+$ T cells were isolated from cell suspension using the EasySep mouse CD8$^+$ T cell isolation kit (Stemcell, 19853), following the manufacturer's instructions. Next, CD8$^+$ T cells were incubated with interleukin (IL) 2 (10 ng/mL), anti-CD3 antibody (5 μg/mL, eBioscience), and anti-CD28 antibody (5 μg/mL, eBioscience) for 72 h.

Transwell co-culture system

The activated CD8$^+$ T cells were obtained as described above. The AML12 cells and PHCs were pretreated with tumor cell culture supernatant for 24 h. The transwell system was inoculated with AML12 cells or PHCs and activated CD8$^+$ T cells. AML12 cells and PHCs were cultured in a 24-well plate. The upper chamber of the transwell (5 μm, Corning) was inoculated with activated CD8$^+$ T cells (5×10^5 cells). After 12 h, the supernatant was collected from the lower chamber of the transwell system. The supernatant was centrifuged to obtain cells, which were stained with Zombie Aqua (BioLegend, 423102) and CD8α (BioLegend, 100708). The number of migrated T cells was determined using a flow cytometer (cytoFLEX, Beckman).

In vitro CD8+ T cell cytokine detection and cytotoxicity assay

The activated CD8$^+$ T cells were obtained as described above. The AML12 cells and PHCs were pretreated with tumor cell culture supernatant for 24 h. The activated CD8$^+$ T cells were co-cultured with PHCs or AML12 cells for 24 h. Some CD8$^+$ T cells were stained with LIVE/DEAD Fixable Blue and antibodies against CD45.2, CD8α, IFNγ, TNFα, and GzmB as described above. CD8$^+$ T cell cytokines were detected using Cytek Aurora (CytekBiosciences). After co-culture with PHCs or AML12 cells, some CD8$^+$ T cells were co-cultured with Hepa1-6 cells (ratio 1:1) for 48 h. Next, Hepa1-6 cells were collected and their concentration was adjusted to 1×10^6 cells. The cells were incubated with 10 μL of allophycocyanin-conjugated annexin V and 10 μL phycoerythrin-conjugated propidium iodide staining solution (ESscience, China) at room temperature for 5 min in the dark. Apoptosis was detected using a flow cytometer (cytoFLEX, Beckman) to test the cytotoxicity of CD8$^+$ T cells.

ELISA and inflammation antibody array

The concentrations of the CX3CL1 and CXCL13 in the culture supernatants or mouse serum were measured using the ELISA kits (Meimian, MM-44874M1; Meimian, MM-45471M1), following the manufacturer's instructions. Additionally, the serum concentrations of inflammatory cytokines in *Ythdf2*$^{F/F}$ and *Ythdf2*^{LKO} mice after tumor inoculation were measured using the mouse inflammation array G1 (RayBiotech, AAM-INF-G1-4), following the manufacturer's instructions.

Lentivirus construction and transfection

The PLKO.1-puro vector was used to clone the short-hairpin RNA (shRNA) targeting *Ythdf2*. *Ythdf2*, *Cx3cl1*, and *Irf3* sequences were cloned into the pSIN-EF2-puro vector. Ythdf2 mutant (W432A) was generated using site-directed mutagenesis. The recombinant plasmids and two virus-packaging plasmids (psPAX2 and pMD2.G) were co-transfected into 293T cells using Lipofectamine 3000 (Invitrogen). Viral particles were packaged in 293T cells and used to infect AML12 cells using Lipofectamine 3000 (Invitrogen). The recombinant cells were selected using puromycin. The efficacy of KD or overexpression was confirmed at both the mRNA and protein levels. The following shRNA sequences were used in this study: shYTHDF2_1, GCAAACTTGCAGTTTATGTAT; shYTHDF2_2, CCATGCCCTATCTAACTTCTT.

The siRNAs targeting *Cx3cl1* and *Irf3* were transiently transfected into AML12 cells using Lipofectamine RNAiMAX (Invitrogen), following the manufacturer's instructions. All siRNA duplexes were obtained from RiboBio (Guangzhou, P.R. China).

mRNA stability assay

AML12 cells were treated with 5 μg/mL actinomycin D (Selleck), a transcription inhibitor, for different durations (0, 1, 2, and 3 h). Total RNA was extracted from cultured cells with an RNA quick purification kit (EScience, China), following the manufacturer's instructions. The mRNA levels were examined using qRT-PCR analysis. The half-life ($t_{1/2}$) of mRNA was calculated using the following equation: $t_{1/2}$ = In 2/*k* (*k* = (In N_0 _ In N_t)/(t _ 0); N_t and N_0 are the RNA quantities at time t and time 0).

RIP assay

The RIP assay was performed as described previously [50]. Briefly, 2×10^7 AML12 cells expressing YTHDF2_WT and YTHDF2_MUT were lysed in a RIP buffer (150 mM KCl, 25 mM Tris-HCl (pH 7.4), 5 mM EDTA, 0.5% NP-40, 0.5 mM dithiothreitol, 1:100 protease inhibitor cocktail (Thermo Fisher Scientific), and 100 U/mL RNase inhibitor (Thermo Fisher Scientific)). The cell lysate was incubated with P/AG beads and anti-YTHDF2 antibodies (Abcam, ab220163) at 4 °C overnight. The beads were washed with NT2 buffer and resuspended into 100 μL. Next, the resuspended beads were incubated with DNase I (20 U) at 37 °C for 30 min, followed by incubation with protease K (50 μg) at 55 °C for 30 min. Finally, bound RNAs were extracted using TRIzol reagent and subjected to qRT-PCR analysis.

Dual-luciferase reporter assays

The 3′ UTR fragments of *Cx3cl1* containing putative m^6A motifs were subcloned into the luciferase reporter vector pmirGLO (Promega). Control, shYTHDF2_1-transfected, shYTHDF2_2-transfected, vector control-transfected, wild-type Ythdf2 overexpression construct-transfected, or mutant YTHDF2 overexpression construct-transfected AML12 cells were transfected with pmirGLO-CX3CL1_3′UTR. To perform the promoter activity assay, the *Ythdf2* or *Cx3cl1* promoter was subcloned into the luciferase reporter vector pGL4 (Promega). Control, shYTHDF2_1-transfected, or shYTHDF2_2-transfected AML12 cells were transfected with pGL4-*Cx3cl1*_pro. AML12 cells were co-transfected with pGL4-*Ythdf2*_pro and pSIN-IRF3. The pRL-TK *Renilla* luciferase reporter was transfected for normalization of transfection efficiency. At 48 h post-transfection, the dual-luciferase reporter assay system (Promega) was used to measure the activities of the firefly and Renilla luciferases. Renilla luciferase activity was normalized to the firefly luciferase activity, and the results were presented as relative luciferase activity.

ChIP assay

ChIP assays were performed using the d EZ-Magna ChIP kits (Sigma-Aldrich, 17-10086), following the manufacturer's instructions. Briefly, AML12 cells were pretreated with vehicle, OXA(4 μg/mL), SN-011 (10 μM), or DMXAA (10 μM) for 24 h. AML12 cells overexpressing IRF3-Flag or silence IRF3 were collected. Cells (1×10^7 cells) were cross-linked with 1% formaldehyde at 37 °C for 10 min and quenched with 0.125 M glycine. After cell lysis, cross-linked chromatin was sheared using Qsonica* Q700 (USA) (10 s on/50 s off for 10 cycles). Sonicated chromatin was immunoprecipitated with 10 μL of anti-Flag antibodies (Cell Signaling Technology, 14793), anti-IRF3 antibodies (Proteintech 11312-1-AP) or corresponding rabbit IgG (Cell Signaling Technology, 2729) at 4 °C overnight. After the reversal of crosslinking, the DNA immunoprecipitated with the indicated antibody was subjected to qRT-PCR analysis using the following primers: Site 1_F: ATATTCCTGCATGAGTTG, Site 1_R: TAAGTAATGTGCCCAAGT; Site 2_F: GCTTCCGCTC CTCCAATC, Site 2_R: ATGGTACTAGAAGAGCCCAA GA.

RNA sequencing

Total RNA was extracted from peritumoral tissues of $Ythdf2^{F/F}$ and $Ythdf2^{LKO}$ mice. RNA sequencing was performed by Yuan Shen Technology (Shanghai, China). Differentially expressed genes were identified and subjected to KEGG pathway analysis using the Majorbio Cloud Platform. The criteria for selecting differentially expressed genes were as follows: $P < 0.05$ and Log_2(fold change) > 1 or Log_2(fold change) < – 1.

Statistical analysis

The statistical tests used in this study are included in the figure legends. The results are expressed as mean ± standard deviation. Means between two groups were compared using unpaired or paired (for the matched group) two-tailed Student's t-test or nonparametric Mann-Whitney U-test. Overall survival and recurrence-free survival were compared using the log-rank test. Pearson correlation was calculated to determine the correlation between parameters. All statistical analyses were performed using GraphPad Prism 8 (GraphPad Software), Statistical Product and Service Solutions (SPSS version 25.0, Inc., Chicago, USA), and R software (R version 4.1.1, R Foundation, Vienna, Austria). Differences were considered significant at $P < 0.05$.

Supplementary Information

The online version contains supplementary material available at https://doi.org/10.1186/s12943-024-02097-6.

Supplementary Material 1

Supplementary Material 2

Supplementary Material 3

Supplementary Material 4

Supplementary Material 5

Supplementary Material 6

Supplementary Material 7

Supplementary Material 8

Supplementary Material 9

Acknowledgements

Authors thank Bullet Edits Limited for the linguistic editing and proofreading of the manuscript.

Author contributions

Z.-Y. Yang: Conceptualization, data curation, formal analysis, validation, investigation, visualization, methodology, writing–original draft, writing–reviewand editing. X.Wang: Conceptualization, data curation, formal analysis, funding acquisition, validation, investigation, writing–original draft, writing–review and editing. Y.-Z. Fu, W.-J. Wu: Resources, data curation, validation, methodology, funding acquisition, writing–review and editing. Z.-L. Hu, Q.-Y. Lin: Data curation, investigation, methodology. W. Peng: Data curation, investigation methodology. Y.-X. Pan, J.-C. Wang, J.-B. Chen: Data curation, visualization. D.-D. Hu, Z.-G. Zhou, L. Xu Y.-J. Zhang: Data curation, supervision, methodology. J.-J. Hou: Conceptualization, resources, supervision, methodology, project administration, writing–review and editing. M.-S. Chen: Conceptualization, resources, data curation, supervision, funding acquisition, methodology, project administration, writing–review and editing.

Fundings

This work is funded by the Guangdong Provincial Science Fund for Distinguished Young Scholars (2021B1515020007, to J.Hou), the National Natural Science Foundation of China (No: 81874070 to M.S. Chen, 82073243 to X. Wang, 82103566 to D.D. Hu), Guangdong Basic and Applied Basic Research Foundation (2022A1515110961 to J.C. Wang), Guangzhou Science and Technology Plan Project (2023A04J2125 to J.C. Wang), the China Postdoctoral Science Foundation (No: 2023M744018 to Y.Z. Fu).

Data availability

No datasets were generated or analysed during the current study.

Declarations

Ethical approval

The experiments including human tissues were approved by the institutional review board of Sun Yat-sen University Cancer Center (approval number: B2024-178-01). All animal experiments were approved by the Laboratory Animal Ethics Committee of Sun Yat-sen University (approval number: L025501202203019).

Competing interests

The authors declare no competing interests.

Received: 17 April 2024 / Accepted: 21 August 2024
Published online: 06 September 2024

References

1. Forner A, Reig M, Bruix J. Hepatocellular carcinoma. Lancet. 2018;391(10127):1301–14.
2. Zhou H, Liu Z, Wang Y, Wen X, Amador EH, Yuan L, et al. Colorectal liver metastasis: molecular mechanism and interventional therapy. Signal Transduct Target Ther. 2022;7(1):70.
3. Li X, Ramadori P, Pfister D, Seehawer M, Zender L, Heikenwalder M. The immunological and metabolic landscape in primary and metastatic liver cancer. Nat Rev Cancer. 2021;21(9):541–57.
4. Hou J, Zhang H, Sun B, Karin M. The immunobiology of hepatocellular carcinoma in humans and mice: basic concepts and therapeutic implications. J Hepatol. 2020;72(1):167–82.
5. Gu Y, Wu X, Zhang J, Fang Y, Pan Y, Shu Y, et al. The evolving landscape of N(6)-methyladenosine modification in the tumor microenvironment. Mol Ther. 2021;29(5):1703–15.
6. Nie S, Zhang L, Liu J, Wan Y, Jiang Y, Yang J, et al. ALKBH5-HOXA10 loop-mediated JAK2 m6A demethylation and cisplatin resistance in epithelial ovarian cancer. J Exp Clin Cancer Res. 2021;40(1):284.
7. Wu Y, Wang Z, Han L, Guo Z, Yan B, Guo L, et al. PRMT5 regulates RNA m6A demethylation for doxorubicin sensitivity in breast cancer. Mol Ther. 2022;30(7):2603–17.
8. Kudo M, Kawamura Y, Hasegawa K, Tateishi R, Kariyama K, Shiina S, et al. Management of Hepatocellular Carcinoma in Japan: JSH Consensus statements and recommendations 2021 Update. Liver Cancer. 2021;10(3):181–223.
9. Zhou J, Sun H, Wang Z, Cong W, Wang J, Zeng M, et al. Guidelines for the diagnosis and Treatment of Hepatocellular Carcinoma (2019 Edition). Liver Cancer. 2020;9(6):682–720.
10. Tsilimigras DI, Brodt P, Clavien PA, Muschel RJ, D'Angelica MI, Endo I, et al. Liver metastases. Nat Rev Dis Primers. 2021;7(1):27.
11. Fu Y, Peng W, Zhang W, Yang Z, Hu Z, Pang Y, et al. Induction therapy with hepatic arterial infusion chemotherapy enhances the efficacy of lenvatinib and pd1 inhibitors in treating hepatocellular carcinoma patients with portal vein tumor thrombosis. J Gastroenterol. 2023;58(4):413–24.
12. Mei J, Tang YH, Wei W, Shi M, Zheng L, Li SH, et al. Hepatic arterial infusion Chemotherapy Combined with PD-1 inhibitors plus Lenvatinib Versus PD-1 inhibitors plus Lenvatinib for Advanced Hepatocellular Carcinoma. Front Oncol. 2021;11:618206.
13. Ganesh K, Stadler ZK, Cercek A, Mendelsohn RB, Shia J, Segal NH, et al. Immunotherapy in colorectal cancer: rationale, challenges and potential. Nat Rev Gastroenterol Hepatol. 2019;16(6):361–75.
14. Biller LH, Schrag D. Diagnosis and treatment of metastatic colorectal Cancer: a review. JAMA. 2021;325(7):669–85.
15. Emens LA, Middleton G. The interplay of immunotherapy and chemotherapy: harnessing potential synergies. Cancer Immunol Res. 2015;3(5):436–43.
16. Obeid M, Tesniere A, Ghiringhelli F, Fimia GM, Apetoh L, Perfettini JL, et al. Calreticulin exposure dictates the immunogenicity of cancer cell death. Nat Med. 2007;13(1):54–61.
17. Deng X, Qing Y, Horne D, Huang H, Chen J. The roles and implications of RNA m(6)a modification in cancer. Nat Rev Clin Oncol. 2023;20(8):507–26.
18. Lin X, Wang Z, Yang G, Wen G, Zhang H. YTHDF2 correlates with tumor immune infiltrates in lower-grade glioma. Aging. 2020;12(18):18476–500.
19. Su G, Liu T, Han X, Sun H, Che W, Hu K, et al. YTHDF2 is a potential Biomarker and Associated with Immune infiltration in kidney renal clear cell carcinoma. Front Pharmacol. 2021;12:709548.
20. Tsuchiya K, Yoshimura K, Inoue Y, Iwashita Y, Yamada H, Kawase A, et al. YTHDF1 and YTHDF2 are associated with better patient survival and an inflamed tumor-immune microenvironment in non-small-cell lung cancer. Oncoimmunology. 2021;10(1):1962656.
21. Ma S, Sun B, Duan S, Han J, Barr T, Zhang J, et al. YTHDF2 orchestrates tumor-associated macrophage reprogramming and controls antitumor immunity through CD8(+) T cells. Nat Immunol. 2023;24(2):255–66.
22. Hou J, Zhang H, Liu J, Zhao Z, Wang J, Lu Z, et al. YTHDF2 reduction fuels inflammation and vascular abnormalization in hepatocellular carcinoma. Mol Cancer. 2019;18(1):163.
23. Moya IM, Castaldo SA, Van den Mooter L, Soheily S, Sansores-Garcia L, Jacobs J, et al. Peritumoral activation of the Hippo pathway effectors YAP and TAZ suppresses liver cancer in mice. Science. 2019;366(6468):1029–34.
24. Lyu N, Kong Y, Mu L, Lin Y, Li J, Liu Y, et al. Hepatic arterial infusion of oxaliplatin plus fluorouracil/leucovorin vs. sorafenib for advanced hepatocellular carcinoma. J Hepatol. 2018;69(1):60–9.
25. Li QJ, He MK, Chen HW, Fang WQ, Zhou YM, Xu L, et al. Hepatic arterial infusion of Oxaliplatin, Fluorouracil, and Leucovorin Versus Transarterial

Chemoembolization for large Hepatocellular Carcinoma: a Randomized Phase III Trial. J Clin Oncol. 2022;40(2):150–60.
26. Gao X, Lei G, Wang B, Deng Z, Karges J, Xiao H, et al. Encapsulation of platinum prodrugs into PC7A polymeric nanoparticles combined with Immune Checkpoint inhibitors for therapeutically enhanced Multimodal Chemotherapy and Immunotherapy by activation of the STING pathway. Adv Sci (Weinh). 2023;10(4):e2205241.
27. Li K, Gong Y, Qiu D, Tang H, Zhang J, Yuan Z et al. Hyperbaric oxygen facilitates teniposide-induced cGAS-STING activation to enhance the antitumor efficacy of PD-1 antibody in HCC. J Immunother Cancer. 2022;10(8).
28. Panigrahi S, Chen B, Fang M, Potashnikova D, Komissarov AA, Lebedeva A, et al. CX3CL1 and IL-15 promote CD8 T cell chemoattraction in HIV and in atherosclerosis. PLoS Pathog. 2020;16(9):e1008885.
29. Yang M, Lu J, Zhang G, Wang Y, He M, Xu Q et al. CXCL13 shapes immunoactive tumor microenvironment and enhances the efficacy of PD-1 checkpoint blockade in high-grade serous ovarian cancer. J Immunother Cancer. 2021;9(1).
30. Liu Y, He S, Wang XL, Peng W, Chen QY, Chi DM, et al. Tumour heterogeneity and intercellular networks of nasopharyngeal carcinoma at single cell resolution. Nat Commun. 2021;12(1):741.
31. Zhu T, Roundtree IA, Wang P, Wang X, Wang L, Sun C, et al. Crystal structure of the YTH domain of YTHDF2 reveals mechanism for recognition of N6-methyladenosine. Cell Res. 2014;24(12):1493–6.
32. Xiang Y, Laurent B, Hsu CH, Nachtergaele S, Lu Z, Sheng W, et al. RNA m(6)a methylation regulates the ultraviolet-induced DNA damage response. Nature. 2017;543(7646):573–6.
33. Maman S, Witz IP. A history of exploring cancer in context. Nat Rev Cancer. 2018;18(6):359–76.
34. Xu M, Zhang T, Xia R, Wei Y, Wei X. Targeting the tumor stroma for cancer therapy. Mol Cancer. 2022;21(1):208.
35. Ozga AJ, Chow MT, Luster AD. Chemokines and the immune response to cancer. Immunity. 2021;54(5):859–74.
36. Zhang W, Zhang Q, Yang N, Shi Q, Su H, Lin T, et al. Crosstalk between IL-15Rα(+) tumor-associated macrophages and breast cancer cells reduces CD8(+) T cell recruitment. Cancer Commun (Lond). 2022;42(6):536–57.
37. Zhang C, Huang S, Zhuang H, Ruan S, Zhou Z, Huang K, et al. YTHDF2 promotes the liver cancer stem cell phenotype and cancer metastasis by regulating OCT4 expression via m6A RNA methylation. Oncogene. 2020;39(23):4507–18.
38. Zhong L, Liao D, Zhang M, Zeng C, Li X, Zhang R, et al. YTHDF2 suppresses cell proliferation and growth via destabilizing the EGFR mRNA in hepatocellular carcinoma. Cancer Lett. 2019;442:252–61.
39. Chen M, Wei L, Law CT, Tsang FH, Shen J, Cheng CL, et al. RNA N6-methyladenosine methyltransferase-like 3 promotes liver cancer progression through YTHDF2-dependent posttranscriptional silencing of SOCS2. Hepatology. 2018;67(6):2254–70.
40. Dixit D, Prager BC, Gimple RC, Poh HX, Wang Y, Wu Q, et al. The RNA m6A reader YTHDF2 maintains Oncogene expression and is a targetable dependency in Glioblastoma Stem cells. Cancer Discov. 2021;11(2):480–99.
41. Yang Y, Yan Y, Yin J, Tang N, Wang K, Huang L, et al. O-GlcNAcylation of YTHDF2 promotes HBV-related hepatocellular carcinoma progression in an N(6)-methyladenosine-dependent manner. Signal Transduct Target Ther. 2023;8(1):63.
42. Wang L, Dou X, Chen S, Yu X, Huang X, Zhang L, et al. YTHDF2 inhibition potentiates radiotherapy antitumor efficacy. Cancer Cell. 2023;41(7):1294–e3088.
43. Zhang TQ, Geng ZJ, Zuo MX, Li JB, Huang JH, Huang ZL, et al. Camrelizumab (a PD-1 inhibitor) plus apatinib (an VEGFR-2 inhibitor) and hepatic artery infusion chemotherapy for hepatocellular carcinoma in Barcelona Clinic Liver Cancer stage C (TRIPLET): a phase II study. Signal Transduct Target Ther. 2023;8(1):413.
44. Rha SY, Oh DY, Yañez P, Bai Y, Ryu MH, Lee J, et al. Pembrolizumab plus chemotherapy versus placebo plus chemotherapy for HER2-negative advanced gastric cancer (KEYNOTE-859): a multicentre, randomised, double-blind, phase 3 trial. Lancet Oncol. 2023;24(11):1181–95.
45. Xu J, Jiang H, Pan Y, Gu K, Cang S, Han L, et al. Sintilimab Plus Chemotherapy for Unresectable gastric or gastroesophageal Junction Cancer: the ORIENT-16 randomized clinical trial. JAMA. 2023;330(21):2064–74.
46. Li N, Kang Y, Wang L, Huff S, Tang R, Hui H, et al. ALKBH5 regulates anti-PD-1 therapy response by modulating lactate and suppressive immune cell accumulation in tumor microenvironment. Proc Natl Acad Sci U S A. 2020;117(33):20159–70.
47. Su R, Dong L, Li Y, Gao M, Han L, Wunderlich M, et al. Targeting FTO suppresses Cancer Stem Cell maintenance and Immune Evasion. Cancer Cell. 2020;38(1):79–e9611.
48. Yankova E, Blackaby W, Albertella M, Rak J, De Braekeleer E, Tsagkogeorga G, et al. Small-molecule inhibition of METTL3 as a strategy against myeloid leukaemia. Nature. 2021;593(7860):597–601.
49. Wang JC, Chen DP, Lu SX, Chen JB, Wei Y, Liu XC, et al. PIM2 expression Induced by Proinflammatory Macrophages Suppresses Immunotherapy Efficacy in Hepatocellular Carcinoma. Cancer Res. 2022;82(18):3307–20.
50. Peritz T, Zeng F, Kannanayakal TJ, Kilk K, Eiríksdóttir E, Langel U, et al. Immunoprecipitation of mRNA-protein complexes. Nat Protoc. 2006;1(2):577–80.

Publisher's note